UNSTEADY AND THREE-DIMENSIONAL CFD SIMULATION OF A DARRIEUS TURBINE ON THE ROOF OF A BUILDING

SAMSON VICTOR

A Thesis

In the Department

of

Mechanical, Industrial and Aerospace Engineering

Presented in the Partial Fulfillment of Requirements for the Degree of

MASTER OF APPLIED SCIENCE (MECHANICAL ENGINEERING)

at

Concordia University

Montréal, Québec, **CANADA**

July 2017

CONCORDIA UNIVERSITY
School of Graduate Studies

This is to certify that the thesis prepared

By: Samson Victor

Entitled: Unsteady and three-dimensional CFD simulation of a Darrieus Turbine on the roof of a
         building

and submitted in partial fulfillment of the requirements for the degree of

Master of Applied Science (Mechanical Engineering)

complies with the regulations of the University and meets the accepted standards with respect to
originality and quality.

Signed by the final Examining Committee:

_____ Chair
Dr. Rolf Wuthrich

_____ Examiner
Dr. Radu Grigore Zmeureanu

_____ Examiner
Dr. Ali Dolatabadi

_____ Supervisor
Dr. Marius Paraschivoiu

Approved by: _____

        MASc. Program Director

        Department of Mechanical and Industrial Engineering

_____, 2017   _____

Dean of faculty

ABSTRACT

Unsteady and Three-dimensional CFD Simulation of a Darrieus

Turbine on the Roof of a Building

Samson Victor

The disastrous effect of climate change has motivated scientists and engineers around the world to reduce dependency on fossil fuels. Among many alternative sources of energy, power production by wind energy has increased exponentially for last few years. Along this spectrum, efforts are made to investigate the possibility to install wind turbine on high roof tops. The onsite generation will also help to integrate micro wind turbines with urban areas. The proposed research work focuses on the CFD study of a Vertical Axis Wind Turbine (Troposkien-shaped) mounted on the upstream edge of a building, so that flow acceleration generated by the edge of the building contributes to enhance performance of the turbine. The CFD methodology validation is done by comparison of performance with experimental data. Geometric configuration of Sheldahl's models is used for unsteady 3D flow of roof mounted Troposkien wind turbine. Three different turbine placement positions at different heights are investigated to observe C_p - λ curve sensitivity at various tip speed ratios. Position 1 and Position 2 are at the edge of the building, whereas position 3 is a few meters away from the edge, directed towards the geometric center of a building. To simulate realistic atmospheric wind conditions, wind gradient is imposed at the inlet, with fixed desired velocity pointing to the middle of the wind turbine. Geometry and numerical setup is described in details, along with the obtained results. The optimal placement position of the turbine shows improvement in the power coefficient from 0.33 to 0.4 at low wind speeds.

ACKNOWLEDGEMENTS

CONTENTS

LIST OF FIGURES

LIST OF TABLES

Nomenclature

ρ	Air Density
μ	Dynamic Viscosity of Air
λ	Tip Speed Ratio
C_m	Coefficient of moment
C_p	Coefficient of Power
M	Moment
ω	Angular speed of rotating domain
V_∞	Free stream velocity
H	Height of the building
h	Height of the rotor
R	Radius of the rotor
v	Vertical coordinate of the node
c	Chord length
N	Number of blades
D	Diameter of Rotor

CHAPTER 1: INTRODUCTION

Growing demand of energy has become a critical challenge. Statistics shows that global energy demand has increased almost three times since 1975 and the world energy market, worth around 1.5 trillion dollars is still dominated by fossil fuels [1]. Most of the energy that the developed world consumes is produced from fossil fuel such as coal, oil / petroleum and natural gas. These finite sources are extracted from earth at great environmental cost and lead to air pollution and greenhouse gas emissions. Fossil fuel reserves tend to mainly depend on two important parameters: consumption and price. The Energy Information Administration (EIA) has projected that the energy consumption will increase at an average rate of 1.1% per annum, the numbers can increase from 500 quadrillion Btu in 2006 to 701.6 quadrillion Btu in 2030 [2]. Among the range of human activities that cause the climate change, the biggest cause by far is "Energy Usage". The climate change problem can principally be termed as an energy problem. In the year 2000, the world's greenhouse gas emissions were about 34 billion tons of CO_2 equivalents per year. Figure 1 shows the world divided into eight regions, where each rectangle represents the greenhouse emission of that region [3].

As a result, the disastrous effects of climate change motivated scientists and engineers, around the world to reduce dependency on fossil fuels. Renewable sources (solar, wind, geothermal, hydro, tidal) are considered as alternative energy to fossil fuel. These are inexhaustible energy sources and shown immense potential to fulfill growing energy demand. Among many alternative sources of energy, power production by wind energy has increased exponentially in last few years. Globally installed wind power has increased almost 2000 times in the first fifteen years of twenty first century [4]. The increasing size of conventional wind turbines has resulted in challenges related to noise pollution, vast land demand and high structural steel cost. Along this spectrum, efforts are made to investigate the possibility to install wind turbine on high roof tops. Statistics shows huge power consumption by residential and commercial building. High rise multi growing residential buildings are one of the fastest growing housing segments in the urban areas. In Canada 30% of all secondary energy is consumed in buildings. Of this 30% residential buildings use approximately 16% and commercial buildings account for approximately 14%. Of the residential portion, 18% is used in apartment buildings [5].
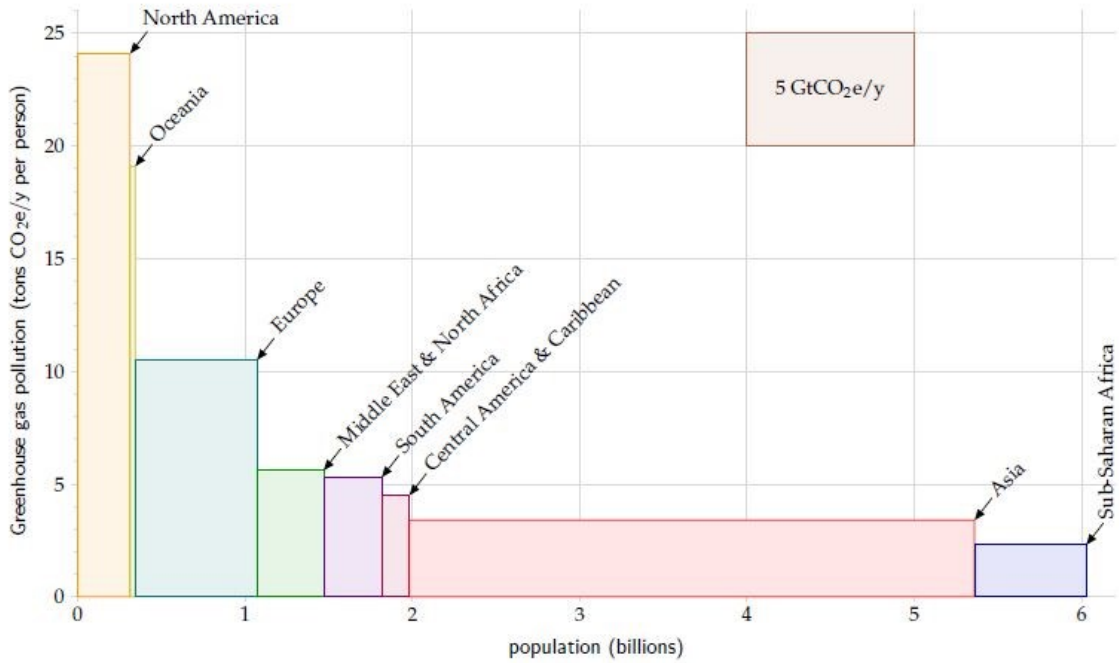
Figure 1: Greenhouse emission per region [3]
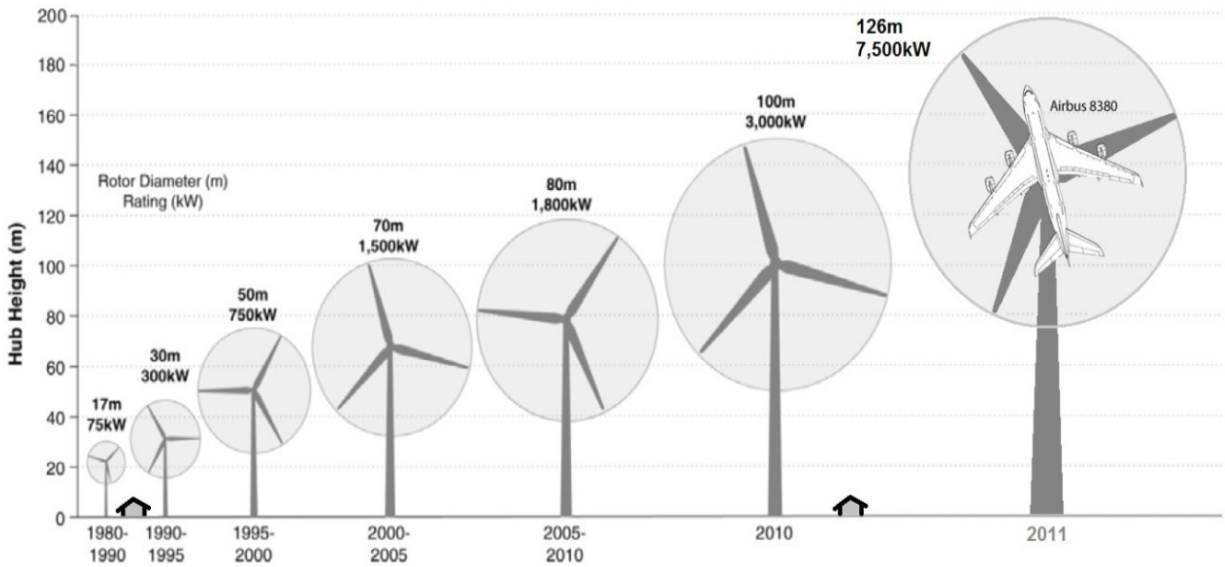
Figure 2: Increasing size of offshore wind turbines

To harness higher wind speeds, the wind turbines sizes are increasing at great extent (Figure 2). When the turbine extracts power from the wind it generates "wake" of turbulence that propagates downwind. This forms the cone shape of slower and more turbulent air. Hence bigger turbines, when placed together in array, need to be further apart to minimize aerodynamic wake effects because it leads to considerable power loss in large wind farms. Sisbot proposed multi objective genetic algorithm for HAWT spacing [6]. The spacing was proposed as a function of rotors diameter "D", it was suggested that minimum distance between two turbines should be 8D in the prevailing wind speed and 2D in the crosswind direction. The roof mounted wind turbines can provide an opportunity for onsite wind generation from wind power, thus reducing transmission losses and high structural cost of massive offshore wind farms. Roof mounted turbines trend will help to integrate micro wind turbines in urban areas. Unfortunately, previous attempts to place wind turbines on roof top have led to low performance, thus optimum positioning of wind turbines needs to be investigated to gain the advantage of wind acceleration from the upstream edge of the building. Among the large family of wind turbines, VAWT wind turbine is suitable choice for roof mounted analysis.

1.1 Objectives

Emphasize Importance of micro wind turbines integration with urban areas

A need of micro wind turbine integration with urban areas is emphasized in introduction and literature review. Several advantages and challenges are highlighted.

Validate methodology with literature review and experimental data

CFD methodology is verified by comparing results with experimental results from Sandia Laboratories and other published text. Chapter 3 is dedicated to this study.

Roof Mounted Wind Turbine Analysis

Chapter 4 deals with the roof mounted wind turbine analysis. A number of objectives are achieved which includes investigating peak power coefficient value sensitivity at different positions. Investigate turbine placement position at upstream edge of the building for optimal performance. Investigate optimum tip speed ratio to achieve power coefficient above baseline configuration of 0.33

1.2 Importance of renewable energy

The estimation of fossil fuels reserves differs in literature due to new explorations and insufficient data on world fossil fuel usage. However more mathematical approach to the fossil fuel reserve depletion can be estimated by fossil fuel rate curves [7]. For years, the uncertainty of fossil fuel timeline has received great attention by private and government sectors. The unconventional renewable energy sources are considered the suitable replacement and renewable energy sector receives the financial, institutional and research support from government. The support comes in form of subsidization schemes, research grants, and feed in tariff/quota systems [8].

Figure 3: Wind Power Global Capacity [9]

Since the transition from conventional to renewable energy sources is inevitable, renewables combined from all sources comprised 30% of world power generating capacity in 2016. After hydropower, wind energy remains the highest contributor to this power generation [9]. Throughout 2016, wind power met 37.6% electricity demand in Denmark and 27% in Ireland. The ongoing growth and geographical expansion of wind energy has made onsite wind power prices competitive to fossil fuel generation due to reduction in component prices.

4

1.3 Types of wind turbines

1.3.1 Airfoil

Airfoil is the shape of the wing or blade and is usually categorized as symmetrical or asymmetric. Symmetric airfoils are shaped the same on both sides as seen in fig.4. They are used to increase the range of angles of attack to avoid spin stall. The Darrieus turbine used for the validation and roof mounted analysis has a symmetric airfoil. The airfoil chosen is the NACA 0012 as suggested by [10] , [11]. It has the thickness of 12% and the chord length of 58.77 mm.

58.77mm

Figure 4: NACA 0012 Airfoil

Recent developments in wind power harvesting have distinguished conventional wind turbines from airborne wind turbines.

1.3.2 Conventional Wind Turbines:

Conventional wind turbines fall into the category of

1   Horizontal Axis Wind Turbines (HAWT)
2   Vertical Axis Wind Turbines (VAWT)

Horizontal Axis Wind turbines: As the name indicates, these turbines have the horizontal rotor shaft and the electrical generators at the back of the blades. This kind of wind turbines require lift force to rotate about the horizontal axis and is also called propeller type turbines.

Vertical Axis Wind turbines: These turbines have the vertical rotor shaft and the generator is placed at the bottom of the turbines. It has the advantage to capture flow from all directions. It is further categorized into Darrieus and Savonius type. A Darrieus Troposkien shaped turbine is shown in figure 5.

Darrieus Type requires the lift force in order for it to rotate, while Savonius are drag based turbines. There are different shapes for Darrieus turbines, which includes Helical, H-Darrieus, and Troposkien etc.

Vertical axis wind turbines are known for their difficulties in self-starting, however there are many advantages as well, that makes them the better choice than horizontal axis wind turbines. The absence of tower makes the installation and maintenance easier, as the generator and major components of the turbine are close to the ground. Other advantages include less noise pollution and longer fatigue of blades [12].

1.3.2.1 Troposkien Wind Turbine

The evolution of VAWT turbines results in curved and straight blade configurations. The term "Troposkien" is defined as "The shape assumed by the perfectly flexible cable of uniform density and cross section if its ends are attached to two points on the vertical axis and it is then spun at constant angular velocity about that vertical axis" [13]. Figure 7 shows the ideal Troposkien shape and its approximation. A practical approximation for the shape was presented by Reis and Blackwell [14]. Straight blade configuration is mostly associated with fixed pitched H-rotor turbine. It is Omni-directional and straight blades are attached to the shaft with horizontal supports. On the other hand, curved blade configuration has been known as phi-rotor. Several variation of phi-rotor is guy-wired, fixed on tower or cantilever shape. Figure 6 shows a guy cable mounted, Sandia's 17 m rotor and component illustration. The phi-rotor is supported by guy wires, thrust bearings at the top and bottom of the rotor. Mechanical brakes are used at the bottom of the rotor shaft to ensure safe operation in strong winds. Torque sensors via flexible coupling were utilized to monitor anomalies in the system and to regulate the generators power. The early design of guy wire exhibited many disadvantages due to complex arrangement and mechanical losses in the component. Figure 5 shows the commercial prototype of the 50 KW and its major components. It does not include the ground mounted stationary shaft but the blade is not manufactured in the multiple small sections. The fixed blade structure reduces the cost of the hydraulic pump and complexity in manufacturing. Considering the Troposkien shape of the structure, it is able to windstand centrifugal forces in strong winds.
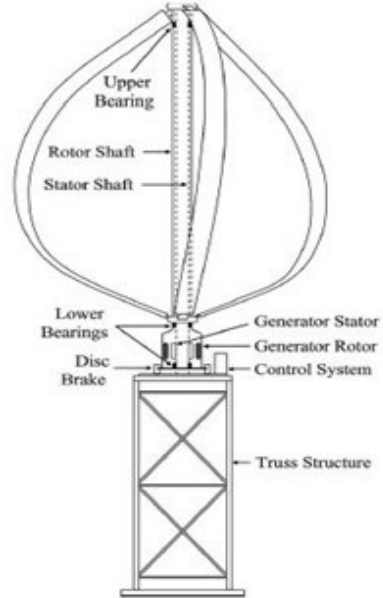
Figure 5: (a) 50KW Rotor manufactured by Arborwind and JSI (b) Artists impression of major components [15]
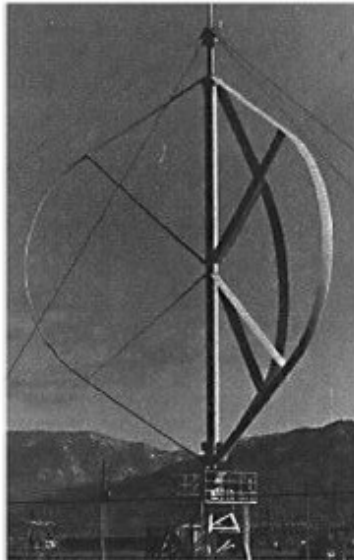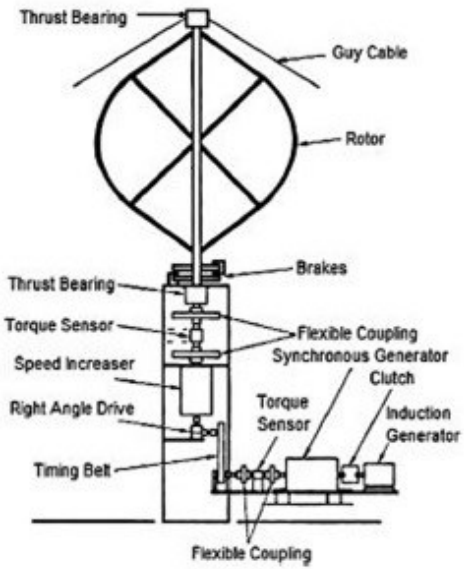
Figure 6: (a) Sandia 17m guy-wired rotor (b) Major component illustration
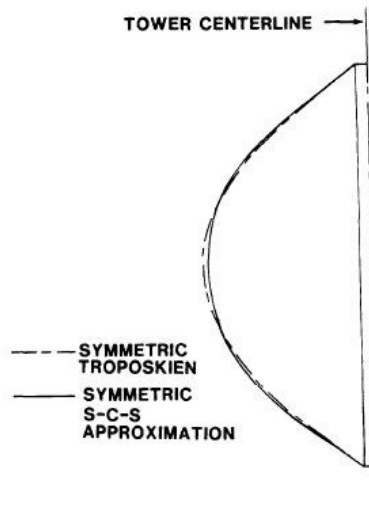
Figure 7: Symmetric Troposkien VS S-C-S Approximation [10]

Reis and Blackwell developed the equation and a computer program "TROP" that describe the Troposkien shape and used as an iterative solution of these equations in the program. Paraschivoiu mentioned that gravity induced stress is related to rotor height to diameter ratio [16]. Lower value of ratio leads to greater gravitational stresses, but variation of airfoil type can be used to minimize gravity and radial aerodynamic interference. Gravity induced bending stress is not required in micro turbines, since blades are shorter and have lower bending moment [15]. There are different versions of Troposkien Shape (1) Ideal Troposkien shape (2) Modified Troposkien Shape (3) Sandia Shape. Ideal Troposkien shape forms the shape of egg beater and also called "skipping rope shape" [10]. Modified Troposkien is achieved by the resolution of integro-differential equation. Analyzing all blade shape for the Darrieus rotor, it can be concluded that parabola shape is a very close approximation of the Ideal Troposkien. Sandia straight circular straight (S-C-S) is a convenient choice. Figure 7 shows the comparison of symmetric Troposkien and S-C-S approximation. Sandia proposed to approximate Troposkien shape with simple shape or combination of shapes that are easy to fabricate. Blades fabricated with S-C-S Troposkien shape are theoretically free of bending stresses caused by centrifugal loads and behaves well structurally.

1.4 VAWT Aerodynamics and Principle of Operation

The CFD analysis of VAWT turbine requires a good understanding of VAWT aerodynamics and operational mechanism. Figure 8 shows the sectioned top view of H-Darrieus wind turbine, although the sectioned view of Troposkien from the middle would be similar. Due to egg beater shape, the maximum radius of Troposkien lies in the middle. The aerodynamics of VAWT is complex due to wide range of angle of attack experienced by the blades in rotational motion. In rotational motion, the blades experience a combination of rotational and incoming wind velocity. From the figure 8 "U" is the velocity from free stream and "W" is the relative velocity of the blade. The term "ωR" is the linear velocity of the blade and is tangent to the circular path of the rotor. The pressure difference around the blade surface generates lift and drag forces. The magnitude of these forces is dependent on angle of attack, magnitude of total apparent wind as well as the shape and chord length of the blade. Breaking down of these forces can also yield the radial and tangential forces as seen in figure 9. It shows the angle of attack and the combination of rotational and free stream flow as seen by the blade. An overall positive thrust is produced when integrating the tangential force around the rotation of the turbine [17].
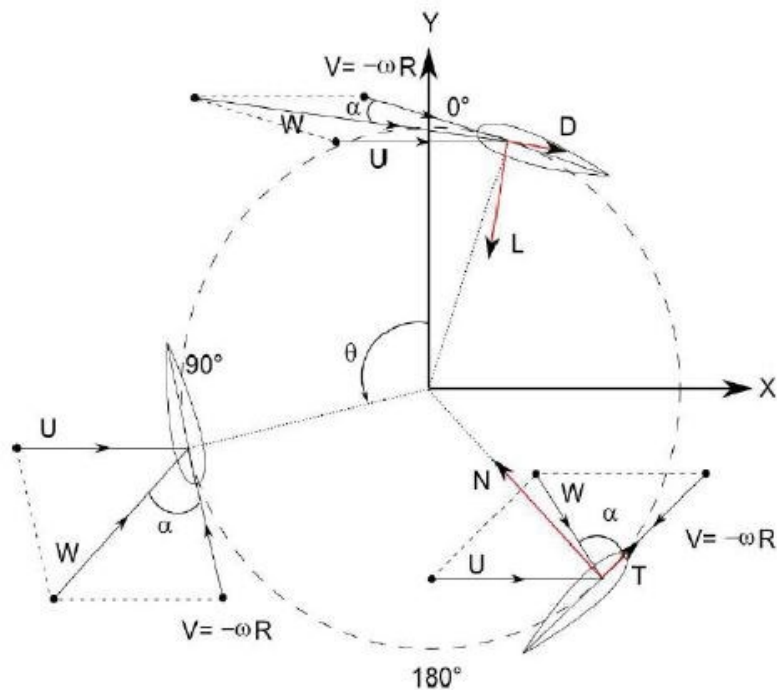
Figure 8: Sectioned view of Vertical Axis Wind Turbine [18]

9
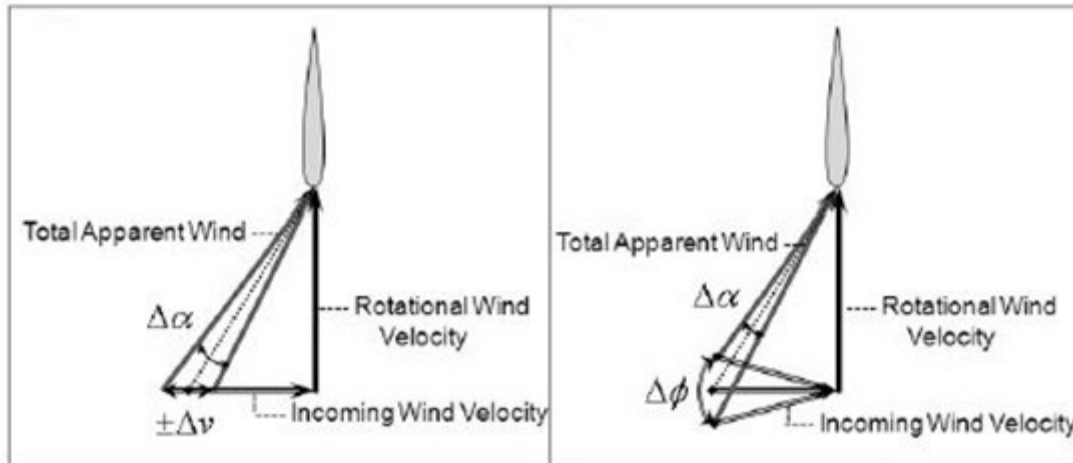
Figure 9: Velocity components breakdown as seen by the blade [17]

For CFD calculations, normal and tangential components are easier to extract due to being normal to the surface. The aerodynamics of wind turbine is complex due to dynamic stall, 3D vortex formation and wake effects affecting the blades in the downstream area. VAWT usually work under high angle of attack compared to horizontal axis wind turbine. Stall occurs at very high angle of attack after the boundary layer separates from the blade surface. The lift force begins to decline and rotational turbulent wakes are generated. High turbulence in the region creates inaccuracy in calculating the downstream blade force. The wind tunnels are widely accepted to study the aerodynamics behavior of VAWT rotor. The challenge of wind tunnel test also includes blockage effects, which arise due to the constrained flow inside the tunnel. This induces artificial acceleration of flow and needs to be corrected to avoid misleading results. Blockage ratio value is usually required less than 3% and is defined as the ratio of the frontal area of the blockage to the cross-sectional area of the wind tunnel [19]. It is desired that the blockage ratio to be as small as possible. Overall the tests and setup cost for wind tunnel test is complex and costly but the increased memory size and processing speed of modern computers allows Computational Fluid Dynamics analysis of full rotors. It provides inexpensive solution to conduct systematic analyses and parametric studies, required for the performance optimization of VAWT.

1.5 VAWT arrangement

Micro-sitting is one of the fundamental problems in wind turbine farm design and the placement of VAWT has received more attention in recent years. The wind farm design requires the wind turbines to be placed in "clusters" or "arrays" but the reduction in spacing between turbines can lead to rapid increase in wake interference. The wake formed downstream can be categorized into near and far wake. The near wake region represents the formation and rolling up of concentrated vortex sheet from rotating airfoil blades. The far wake represents more turbulent wake uncorrelated with the initial disturbance. Far wake region normally represents 5 or more diameters downstream of the rotor.

The wake of HAWT can be compared to aircraft wing, with vortices forming the helix pattern, whereas wake behind the Darrieus starts with the closed latex structure. The wake pattern of HAWT decays slowly with downstream than the wake formed by the vertical axis wind turbines. The wake of Darrieus turbine was studied by Phillips and introduced the vortex model for Darrieus rotor [20]. He concluded that the circular strengths of the vortices in the vortex model depend on the turbine parameter, such as tip speed ratio, solidity, airfoil blade section and blade position relative to incident airstream. The turbines were arranged in an array with a distance of four diameters downstream and rate of rotation was recorded for downstream wind turbines. The velocity deficit at the downstream of the rotor shows reduction of 23.3% than free stream velocity. The experimental study of far wake concluded that turbine should be placed 40 diameters apart to avoid mutual power depreciation greater than 10%. A similar theoretical value was also purposed by Templin: this implies that a 2m rotor should be placed 80m from the upstream rotor. This makes the present approach impractical for places with confined space and a better configuration is needed to allow greater power density for given area.

1.5.1 Flow around a building

Micro wind turbines are defined as the wind turbines with capacity less than 2.5 KW. The onsite generation of building integrated micro wind turbine is gaining more attention. Different attempts have been made around the globe to take advantage of the higher wind velocities on high rise buildings. Figure 10 shows the vertical and horizontal axis wind turbines installed at

the edge of the building. The turbine optimum placement position is investigated in this research. On left, is the VAWT developed by Denmark based Ecofys BV. The manufacturer claims the turbine to be insensitive to speed and direction, due to vertical configuration. Horizontal axis wind turbine is shown on the right hand side. Wind save turbine is based in Edinburgh and designed for use on rooftop, the payback time period is claimed to be less than five years. Figure 11 shows 1.5 KW VAWT and 1 KW horizontal axis wind turbines installed on the Electrical and Mechanical Services department headquarters, Hong Kong. The location is known for high wind potential and densely high rise buildings. These turbines are connected to the grid, using small mounted grid tie inverters [21].

Before installing a wind turbine, it is vital to understand the flow around a building. The evolution of computers allows the Computational wind engineering (CWE) to evaluate the interaction between wind and buildings numerically. This Computational Fluid Dynamics model can be used to identify accelerated flow region and to design and to evaluate the performance of wind turbines of roof top.

(a)   (b)
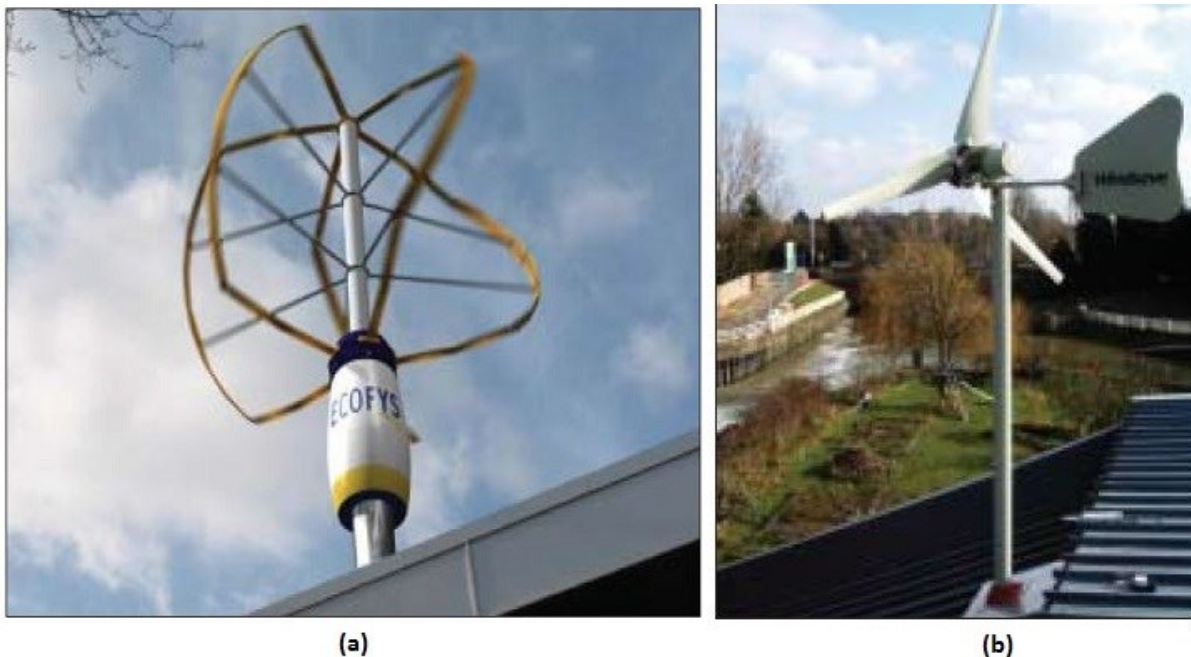
Figure 10: (a) The urban turbine developed by Ecofys (b) The Windsave turbine [21]
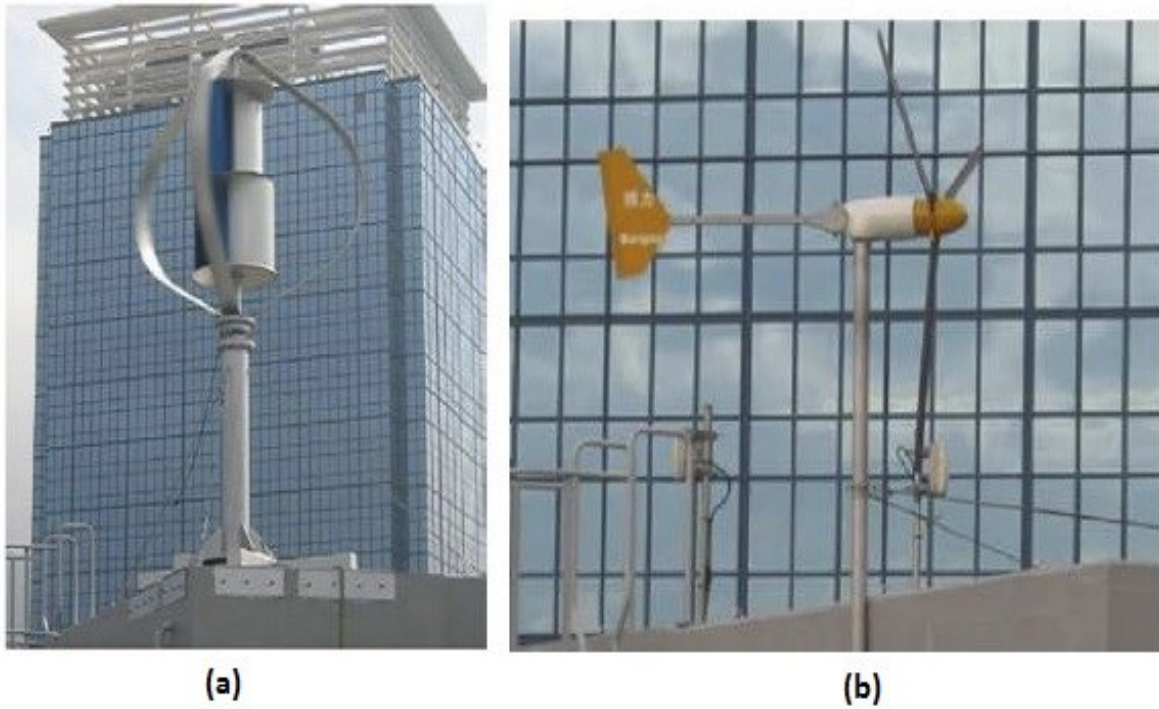
Figure 11: (a) 1.5 KW VAWT (b) 1 KW horizontal axis turbines on roof of EMSD headquarters building of Hong Kong [22]

The flow around a building with a turbine is extensively investigated by Song [23]. The main vortex regions are identified as the recirculation region at the roof top due to the flow acceleration from the upstream edge. The horseshoe vortices around the building, near the ground and the Karman vortices at the building downstream. Figure 12 shows the streamlines at front view of the building. The dimension of the domain and building is taken from [24]. It is the noticed that the flow is undisturbed at the top of the domain and the flow acceleration at the upstream edge and vortices formation is observed at the downstream edge of the building. The study is carried out to identify the flow acceleration region and separation bubble on the roof of the building. The geometry, mesh and numerical setup details are omitted as the subject is extensively covered in literature review [25] , [26].
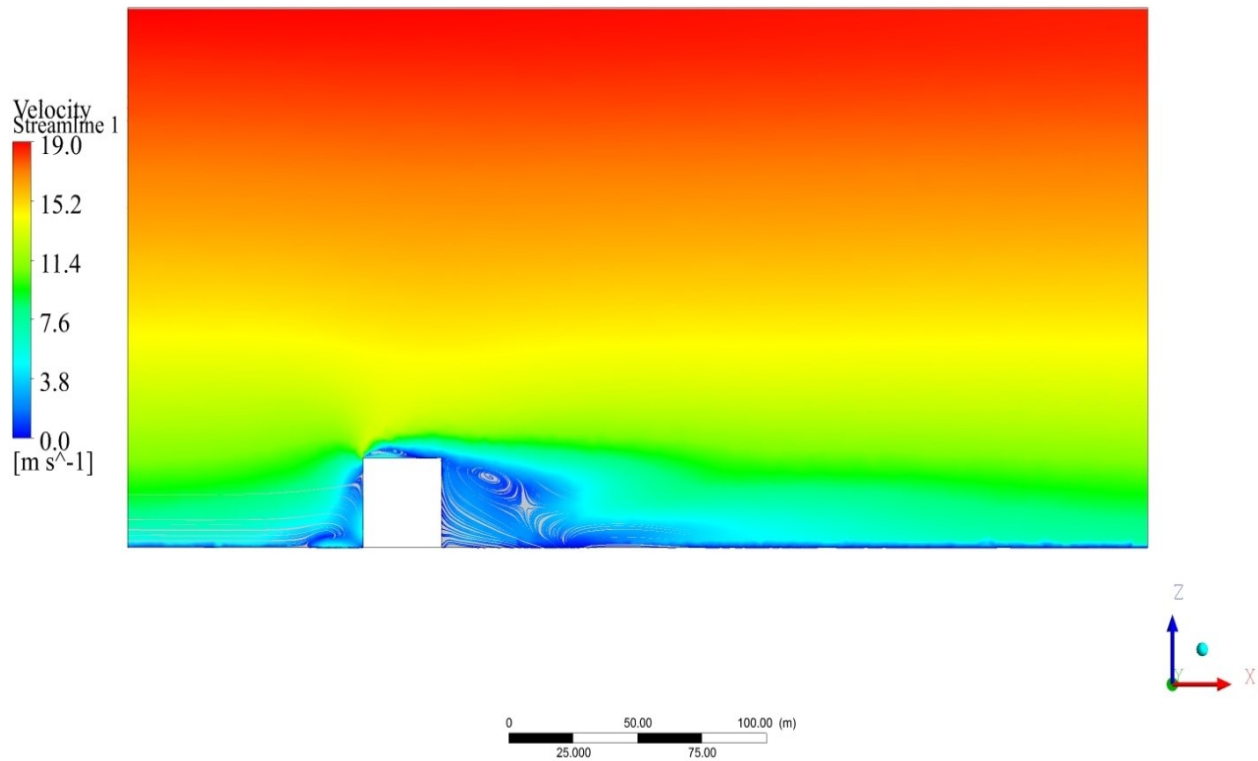
Figure 12: Flow over a building

1.5.1 Fish-schooling formation

The comparative studies of different wind turbine designs purpose that VAWT is capable of producing more power in less space by implying fish schooling method. This characteristic allows VAWT to perform better in the confined areas, makes it a better choice for roof mounted placement. The study is bio-inspired by nature, migrating birds and fishes show that they have
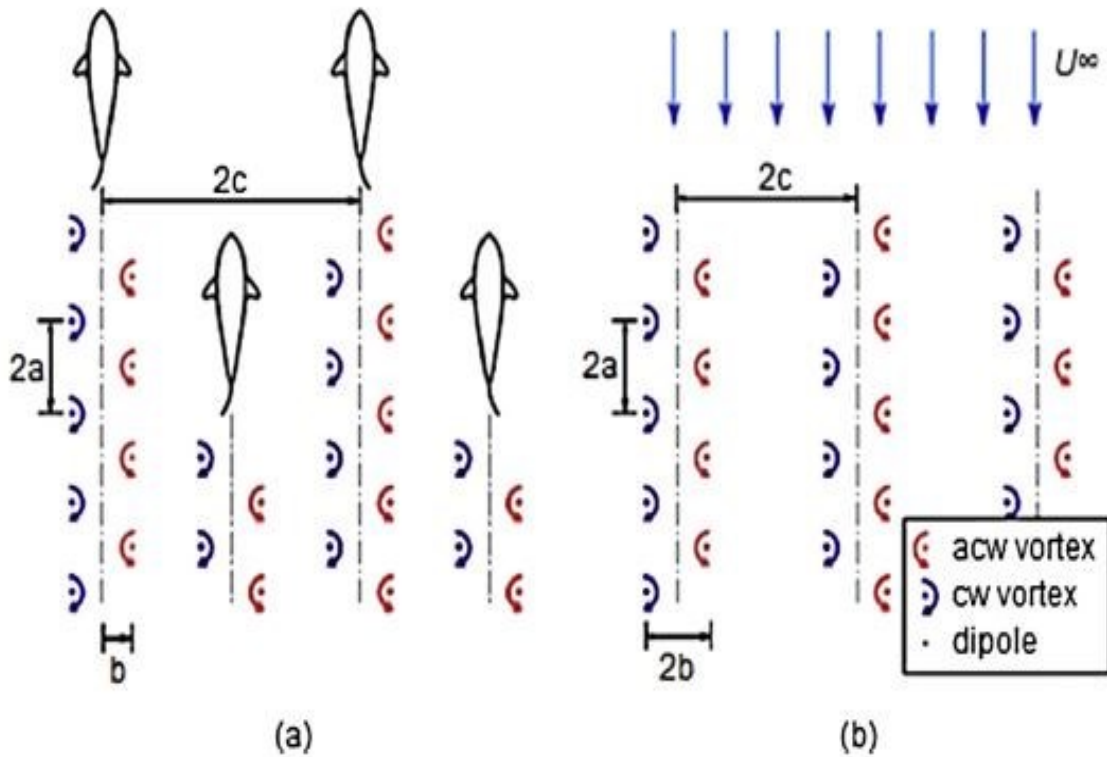
Figure 13: (a) Wake vortices of schooling fish (b) Proposed VAWT farm configuration [27], [17]

more stamina in traveling farther as a group by positing themselves precisely at coordinates [15]. As a result, the animals are able to gain from the vortices shed by animals ahead. The fish schooling pattern was studied by Weihs, he studied hydro dynamical interactions between the fish swimming close to each other in synchronization at equal velocities [28]. Figure 13 shows the bio-mimicry configuration of Darrieus VAWT wind farm based on wake vortices of fish schooling. The clockwise and counter clockwise vortices represent dipoles of wake vortices formed by the school. The distances between the dipoles are indicated by 2a, 2b and 2c. Where 2a represents downstream distance of two vortices, 2b is the lateral distance between the clockwise and anti-clockwise vortex of particular fish and 2c is the distance between two adjacent fishes. It was observed that same rotational direction greatly affects the performance of pair. On the other hand, the performance is generally unaffected by counter rotating turbines. Whittlesey concluded that fish schooling configuration reduced the land use for VAWT wind farm, resulting in array power density increase of over one order of magnitude, compared to operational horizontal wind turbine placements.

15

CHAPTER 2: VAWT MODEL DESCRIPTION

2.1 Important Parameters and Equations

2.1.1 Tip speed ratio

Tip speed ratio is defined as velocity at tip of the blade to the actual wind speed [29]. Where, ωR is the velocity at the tip of the blade, ω is the angular speed of the turbine rotor, measured in rads[-1]. V_{wind} is the free stream velocity of the wind. Higher tip speed results in higher noise levels. It is a dimensionless parameter and denoted by the Greek symbol "λ" or "TSR".

$$\lambda = \frac{\omega R}{V_{wind}} \quad (1)$$

2.1.2 Power Coefficient

Turbine performance is typically based on the relationship between power coefficient and tip speed ratio. Power coefficient is defined as measurement of how the wind turbine converts the energy in the wind into electricity [29], the terms in denominator of eq. 2 represents the power in the wind, it is a function of density, wind velocity and the area intercepting the wind. The factor is a non-linear function of tip speed ratio, therefore changes with wind velocity. Different rotor types have varying range for maximum power coefficient but limited by Betz limit. It is named after German physicist Albert Betz and is the maximum possible conversion efficiency possible (C_p = 0.59). In practice, the value is difficult to obtain and in most instances, it is provided by manufacturer documentation, which are used in many control schemes as look-up tables to generate optimal target power coefficient [30]. The value achieved in practice is also dependent on gear box losses and generator efficiency. Other names for the quantity are power coefficient of the rotor or rotor efficiency.

$$C_p = \frac{M\omega}{0.5\rho V^3 A} \quad (2)$$

2.1.3 Wind Profile

Wind profile is imposed at the inlet boundary and is defined as the relation between wind speed and height [31]. It is called "Atmospheric boundary layer (ABL) or "wind gradient". The formulation is given by

$$V_z = V_{top} * \left(\frac{Z}{H_t}\right)^{0.31} \tag{3}$$

Where Z is the height measured from the ground in meters, H_t is height from the ground to the middle of the rotor. V_{top} is the velocity at desired height (H_t).

2.2 Mesh Setup Review

The mesh setup which includes mesh size and mesh quality determines the computational cost and accuracy of the calculation [12]. The mesh setup is characterized into structured and unstructured mesh. The unstructured grid forms arbitrary shaped elements, this consists of triangular elements in 2D and prism shaped tetrahedral elements in 3D. These elements are known for irregular connectivity and structured elements are identified by regular connectivity. They comprise the shape of quadrilateral in 2D and hexahedral in 3D. Each cell in the grid is directly addressed by the index (i,j) in 2D and (i,j,k) in 3D [32]. This type of mesh is made finer near the wall or area of interest and smoothly increases to bigger elements to reduce computational time. All neighboring states of the cells must be known to calculate the residuals. This can be done easily for structured mesh by adding/subtracting 1 from cell indices, whereas the unstructured mesh requires the storage of cell to cell pointers. In ANSYS Mesher, several factors indicate the quality of the mesh. Some of these are Skewness factor and orthogonal quality. Skewness is defined as the difference between the shape of the cell and the shape of an equilateral volume [33]. Skewness factor less than 0.95 is desired to avoid wrong interpolation and convergence difficulties.

2.2.1 Hybrid mesh

The hybrid mesh is a combination of structured and unstructured meshes. These are widely used in viscous computational fluid dynamic problems, because they allow better control of the cell

size in the computational domain [34]. Hybrid meshes can either be conformal or non-conformal mesh. The non- conformal requires non identical mesh node locations that permit the cell node to be easily connected to each other by passing fluxes from one mesh to another.

This technique is used for both the methodology validation part, and also for the roof mounted wind turbine as suggested in [35]. Two different mesh densities are imposed on the computational domain. The hexahedral or structured mesh is formed around the blade walls to perform the reliable simulation of the boundary layer and non-conformal, smooth mesh transition is made to unstructured or tetrahedral cells. The unstructured mesh helps to capture the cylindrical shape of the rotating domain.

2.3 Wall treatment

The majority of the time spent by engineers on CFD projects in industry is usually devoted to successfully generating the mesh for the domain [36]. The mesh quality near the wall is of high importance as turbulent flows are significantly affected by the presence of the wall. The wall is the main source of vorticity, turbulence and the mean velocity on the wall has to be zero because of the no-slip condition and turbulence is also changed due to wall presence. y+ is a non-dimensional parameter that indicates the distance from the wall. It is given by eq. 4. The near wall region is divided into three layers (Viscous sublayer, buffer layer, fully turbulent region) and shown in figure 14.
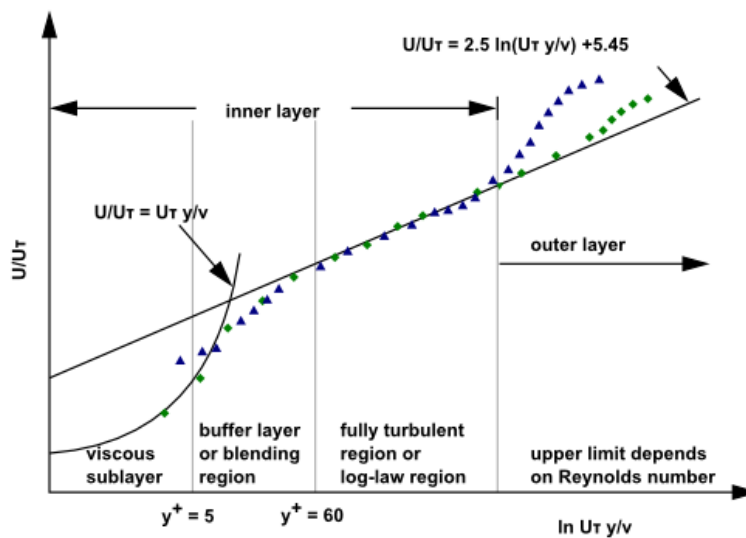
Figure 14: Subdivision of the Near-Wall Region [37]

18

$$y^+ = \frac{y u_\tau}{\nu}$$

(4)

Where u_τ is the frictional velocity and "y" is the normal distance from the wall. The two approaches for wall treatment are

- Wall function
- Near wall treatment.

2.3.1 Wall Function

The wall functions are semi empirical formulas that bridge the flow between the highly viscous flow in the boundary layer and free stream flow, viscous sublayer and buffer layer is not resolved. This wall treatment allows the coarser mesh in the near wall region. The first element y^+ requirement is between 30 and 300 and is suitable for flows with interest in the middle of the domain instead of forces on the wall. The standard or non-equilibrium wall function is recommended for flows with high Reynolds numbers applications ($Re > 10^6$) for which the viscous sublayer resolution is expensive. It is also suggested for mildly separating, reattaching or impinging flow.

2.3.2 Near Wall treatment

This approach resolves the flow all the way to the wall and predicts higher accuracy of flow behavior. Near wall treatment combines the law of the wall and two layer zonal method. It is used for flows with complex near wall phenomena. It requires a fine near wall mesh all the way to the viscous sub-layer, which comes at the expense of high computational cost. The first element y^+ requirement is 1. It is recommended for engineering applications, where flow separation and forces on the wall (i-e aerodynamic drag, lift, etc.) and reattachment are of significant importance. The near wall modeling significantly impacts the fidelity of numerical solutions. The Spalart Allmaras and k-ω models are valid all the way to the top, provided the mesh is refined enough.

2.4 Turbulence Modeling Approach:

Turbulent flow is characterized by the increase in Reynolds number. It is a dimensionless parameter and is given by

$$Re = \frac{\rho u D}{\mu}$$

<div align="right">(5)</div>

Where "D" is the characteristic length, the properties of turbulent flow (density, pressure, velocity etc.) undergo random fluctuations created by the presence of numerous eddies of various sizes and as a result, vary irregularly in space and time, with broad frequency range [38]. The first step towards the categorization of turbulent flow study is to distinguish between the small scale turbulence and the small scale motions in turbulent flows. There are three popular methods to model the turbulent flow

1. Reynolds Averaged Navier Stokes (RANS):
2. Large Eddy Simulation (LES)
3. Direct Numerical Simulation (DNS)

2.4.1 Reynolds Averaged Navier Stokes (RANS)

The governing equations of Navier-Stokes equations are known for over a century. These equations adequately describe the fluid flow behavior and give every detail of turbulent velocity field from the largest to smallest length and time scales. As a consequence, the direct approach of solving the Navier-Stokes equation is impossible [39], RANS is the time averaged equation of motion of fluid flow. In Reynolds averaging, the solution variables in the instantaneous Navier Stokes equations are decomposed into mean and fluctuating components. For the velocity components

$$u_i = \overline{u_i} + u_i{}'$$

<div align="right">(6)</div>

Where $\overline{u_i}$ and $u_i{}'$ are the mean and fluctuating velocity [37]. Similarly for pressure and other scalar quantities

$$P = \bar{P} + P' \tag{7}$$

Substituting expression of this form into instantaneous continuity and momentum equations and taking a time average yields the ensemble averaged momentum equations. This can be written in Cartesian tensor form as

$$\frac{\partial \rho}{\partial t} + \frac{\partial}{\partial x_i}(\rho u_i) = 0 \tag{8}$$

$$\frac{\partial}{\partial t}(\rho u_i) + \frac{\partial}{\partial x_j}(\rho u_i u_j)$$
$$= -\frac{\partial p}{\partial x_i} + \frac{\partial}{\partial x_j}\left[\mu\left(\frac{\partial u_i}{\partial x_j} + \frac{\partial u_j}{\partial x_i} - \frac{2}{3}\delta_{ij}\frac{\partial u_l}{\partial x_l}\right)\right] + \frac{\partial}{\partial x_j}(-\rho\overline{u_i' u_j'}) \tag{9}$$

Eq. 6 and Eq. 7 are known as Reynolds-averaged Navier Stokes equations. The term $-\rho\overline{u_i' u_j'}$ are called Reynolds stresses and must be modeled in order to close the equations (9) [37].

For this thesis, ANSYS Fluent software (Academic 16.2) is used. It is designed to analyze the flow field using Finite Volume Method solution of Navier-Stokes equations. Part of the equation of Navier-Stokes is responsible for

1. Unsteady flow description
2. Convection
3. Diffusion
4. External forces influence on the flow

2.4.2 Large Eddy Simulation (LES)

Since turbulent flows are characterized by eddies with vast range of length and time scales, the LES method is considered in between the RANS and DNS. The large eddies are resolved directly, while small eddies are modeled. This method can be helpful to predict flow accurately as momentum, mass, energy and other passive scalars are transported mostly by large eddies. The resolution of large eddies allows to use coarser mesh and larger time step sizes as compared

to DNS method. However the drawback to use this method is the high resolution requirements for the wall bounded layers, as the larger eddies get small near the wall leading to the increase in both the time and computational cost. It is ideally used for combustion and mixing problems where RANS models fail to meet the needs.

2.4.3 Direct Numerical Simulation (DNS)

Direct numerical simulation is used to study the details of the turbulent flows. This method solves directly the whole spectrum of turbulent scales and does not require any modeling in the setup. However due to high computational cost, this method is not feasible for high Reynolds number flow. The DNS model of ANSYS FLUENT is based on the Sarkar and Hussaini model for the simulation of the isotropic turbulence [37].

2.5 Boundary Conditions

Boundary conditions setup is crucial part for the simulation setup, wrong or incorrect choice of boundary conditions can lead to divergence or misleading results. Depending on flow properties (compressible or incompressible) ANSYS Fluent offers a broad range of options to choose boundary conditions. The boundary conditions chosen for the numerical setup for validation and roof mounted turbine are discussed in this section.

2.5.1 Velocity Inlet

This boundary condition is used to define the velocities and scale properties of the flow at the inlet. The other options that can be selected at the inlet boundary condition are pressure inlet and mass flow inlet. The uniform velocity inlet is selected for the validation part, while a wind gradient is imposed at the inlet boundary of the roof mounted study. The equation for atmospheric boundary layer is described in section 2.1.3

2.5.2 Symmetry Boundary condition

This type of boundary condition is used when physical geometry of interest and expected pattern of the flow have mirror symmetry. This can be used to model zero shear slip walls in viscous flow.

2.5.3 Pressure Outlet

Similar to velocity inlet, ANSYS fluent offers various options to choose for the outlet boundary condition. This includes outflow boundary condition, pressure far-field and pressure outlet. The "outflow" is used to model flow exits, where details of the flow velocity and pressure are not known prior to the solution of the problem. The "far-field" conditions are used to model the free stream compressible flow at infinity. This boundary condition can only be used for compressible flows. "Pressure Outlet" is used for all the cases of validation and roof mounted wind turbine analysis. This defines static flow at the outlet and often results in better rate of convergence than "outflow" during backflow.

2.6 Spatial and temporal discretization schemes

Each governing equation can be discretized in time and space. The discrete values are stored at the center of the cells and must be interpolated from the cell center walls. It is accomplished using an upwind scheme. Gradients are needed not only for constructing values of a scalar at the cell faces, but also for computing secondary diffusion terms and velocity derivatives. The gradient $\Delta\Phi$ of a given variable Φ is used to discretize the convection and diffusion terms in the flow conservation equation [37].

ANSYS Fluent offers three options for gradient evaluation

1. Green-Gauss Cell-Based;

2. Green-Gauss Node-Based;

3. Least Square Cell-Based.

Least Square Cell-Based is the default choice in the numerical setup. It is computationally less expensive than Green-Gauss Node-Based and is used for all the cases in Chapter 3 and Chapter 4. The solution is assumed to vary linearly and the accuracy of this method is comparable to node based gradient for unstructured meshes. Depending on the turbulence model, upwinding scheme options are available for momentum, turbulent kinetic energy and dissipation rate. First order upwinding scheme is selected with the assumption that cell center values of any field represent a cell average value and hold throughout the entire cell. On the other hand, cell faces

are computed using multidimensional linear reconstruction approach for second order upwind scheme. Similar to Spatial discretization, unsteady simulations require temporal discretization of upwinding scheme. Temporal discretization can either be first order or second order implicit. Since a second order implicit scheme is computationally expensive and takes longer to converge, first order implicit is used for all the calculation of validation and roof mounted wind turbine analysis.

2.7 Pressure Velocity coupling schemes

Pressure-velocity coupling schemes refers to the numerical algorithm which uses the combination of continuity and momentum equations to derive equation for pressure [37]. Continuity equation is reformatted as a result. The Pressure based solver solves the flow in either segregated or coupled manner. There are four algorithms available in FLUENT but the one used for this validation and roof mounted analysis will be discussed

1. Semi-Implicit Method for Pressure-Linked Equations (SIMPLE);

2. SIMPLE-Consistent (SIMPLEC);

3. Pressure- Implicit with Splitting of Operators (PISO);

4. Coupled.

The first three algorithms in the list are called segregated algorithms. Each governing equations for the solution variables (velocity, pressure, temperature, etc.) are solved one after another. The scheme is also beneficial for memory consumption, since the discretized equation only needs to be stored in the memory one at a time. Unlike the segregated algorithm, the coupled scheme simultaneously solves the momentum equations and pressure based continuity equations. Since the momentum and continuity are solved in a closely coupled manner, the memory consumption increases 1.5 - 2 times compared to the segregated algorithm.

2.7.1 SIMPLE Scheme

The SIMPLE scheme is employed for the pressure velocity coupling for all the cases of validation and roof mounted analysis. Given the time step size and turbulent nature of the flow, it is suggested in [35], for the wind tunnel analysis of half rotor. It is a segregated scheme and solve the solution variable separately. It and was proposed by Patankar and Spalding [40]. In this method, the continuity equation is converted into an equation for the pressure corrector, overturning the linkage between pressure and density to extend applicability range up to zero Mach number. The equations are solved in sequential steps letting the iterative process take care of the non-linearity as well as the coupling between equations [41]. The implicit treatment of the source term in the governing equation of the SIMPLE algorithm, is more appropriate than the alternative pressure-velocity coupling schemes.

CHAPTER 3: METHDOLOGY VALIDATION

3.1 Governing equations

The SST k - ω is used as the turbulence model. It comprises the transport equation for turbulent kinetic energy and specific dissipation rate ω. It is a two equation model and has similar form to that of the standard k - ω standard. It combines the original robust formulation of modified Wilcox equation for use near the wall and the standard k − ε model away from the wall. It is widely used for the boundary layer problems under various pressure gradients and blends the k - ω model for the near wall treatment and k-ε model in the far field. The dependency on wall distance makes it less suitable for free shear flows but beneficial for the improvement of eddy viscosity in the adverse pressure flow region.

$$\frac{\partial}{\partial t}(\rho k) + \frac{\partial}{\partial x_i}(\rho k u_i) = \frac{\partial}{\partial x_j}\left(\Gamma_k \frac{\partial k}{\partial x_j}\right) + G_k - Y_k + S_k \qquad (10)$$

and

$$\frac{\partial}{\partial t}(\rho \omega) + \frac{\partial}{\partial x_i}(\rho \omega u_i) = \frac{\partial}{\partial x_j}\left(\Gamma_\omega \frac{\partial \omega}{\partial x_j}\right) + G_\omega - Y_\omega + D_\omega + S_\omega \qquad (11)$$

$$\Gamma_k = \mu + \frac{\mu_t}{\rho_k} \qquad (12)$$

$$\Gamma_\omega = \mu + \frac{\mu_t}{\rho_\omega} \qquad (13)$$

Where ρ_k and ρ_ω are turbulent Prandtl numbers, these are calculated using the blending function for k and ω and μ_t is turbulent viscosity. The enhanced wall function with k − ε behaves in the same way as k-ω SST.

$G_{k,\omega}$ represent the production of k and ω respectively. G_k shows the turbulent kinetic energy produced due to the mean velocity gradient. Γ_k and Γ_ω represents the effective diffusivity of k and ω. $Y_{k,,\omega}$ denote dissipation of k and ω due to turbulence. S_k and S_ω are user defined source terms. D_ω represents the cross-diffusion term. The y^+ requirement of this model is 1.

3.2 Turbine Geometry

The geometry used for validation is shown in figure 17. Only half of the rotor is shown as a symmetry condition is used for simulation. URANS CFD results are validated against the experimental data results conducted by Sheldahl [11], for a 2 meter height turbine shown in figure 15. The model used for wind tunnel tests also had three blades. The blades attached to the rotating tower were machined from high strength aluminum alloy (7075-T6) to the NACA 0012 airfoil section as a flat ribbon and then formed to the curved shape.

A similar CFD validation was performed by Bedon and Stefano [35]. Similarly to Sheldahl's model, Straight-circular-straight approximation is used for the blade profile. The rotor is 2 meters high with a maximum radius of 0.98m at the middle of the rotor. NACA 0012 with a chord length of 58.77 mm is used for the blade profile as shown in figure 4. The main characteristics of the rotor are given in Table 1.

Table 1: Main Geometric configuration of Sandia tested model

Number of blades	3
R [m]	0.98
h [m]	2
c [m]	0.05877
v [m]	0.5654
Blade profile	NACA 0012

Figure 15: Sandia 2m wind tunnel model [11]
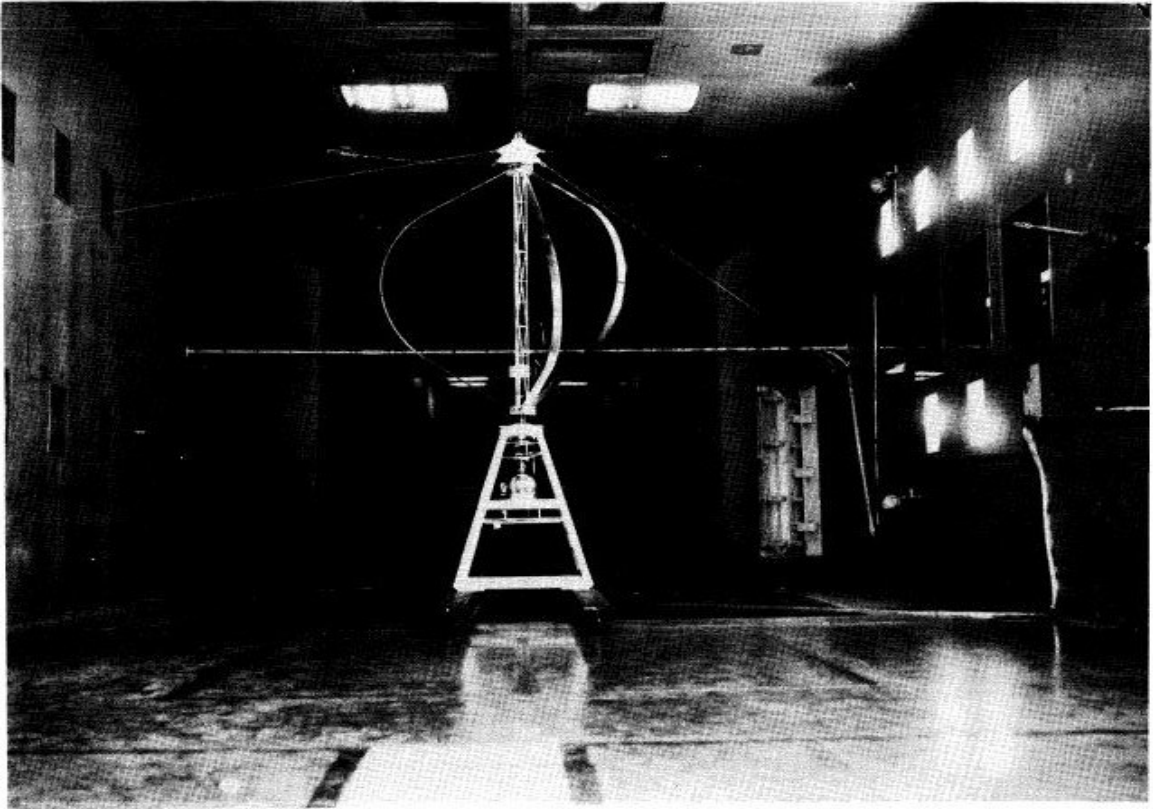
Figure 16: Sandia model at test site [11]
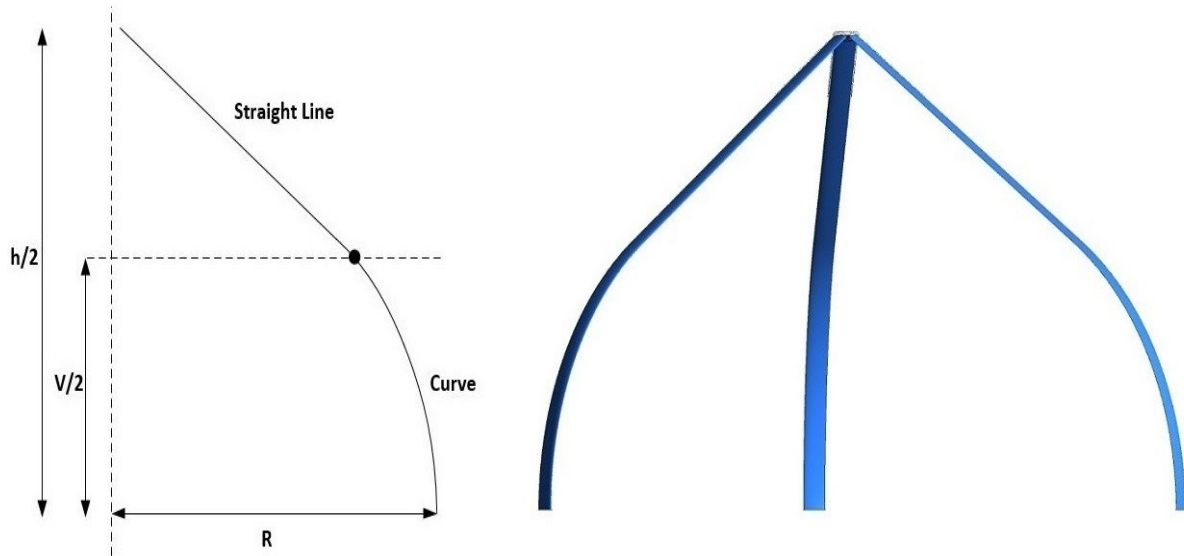
Figure 17: Troposkien geometry details

29

3.3 Computational domain

The dimensions of the computational domain are taken from [35]. The side view of the domain is seen in figure 18. The inlet boundary is placed 30m from the middle of the rotor. The domain is divided into stationary and rotating domain and the rotor is placed in middle of the rotating domain. The rotating domain is shaped as a dome in Bedon's paper, while cylindrical shaped rotating domain is used for this validation. Compared to inlet boundary, the outlet boundary is placed 60m from the middle of the rotor to avoid divergence and reverse flow issues. The height of the rotating domain is 2.5m and the total height of the domain is 3m. The computational domain is extended to 20 m in the lateral direction as seen in the top view of the domain in figure 19.
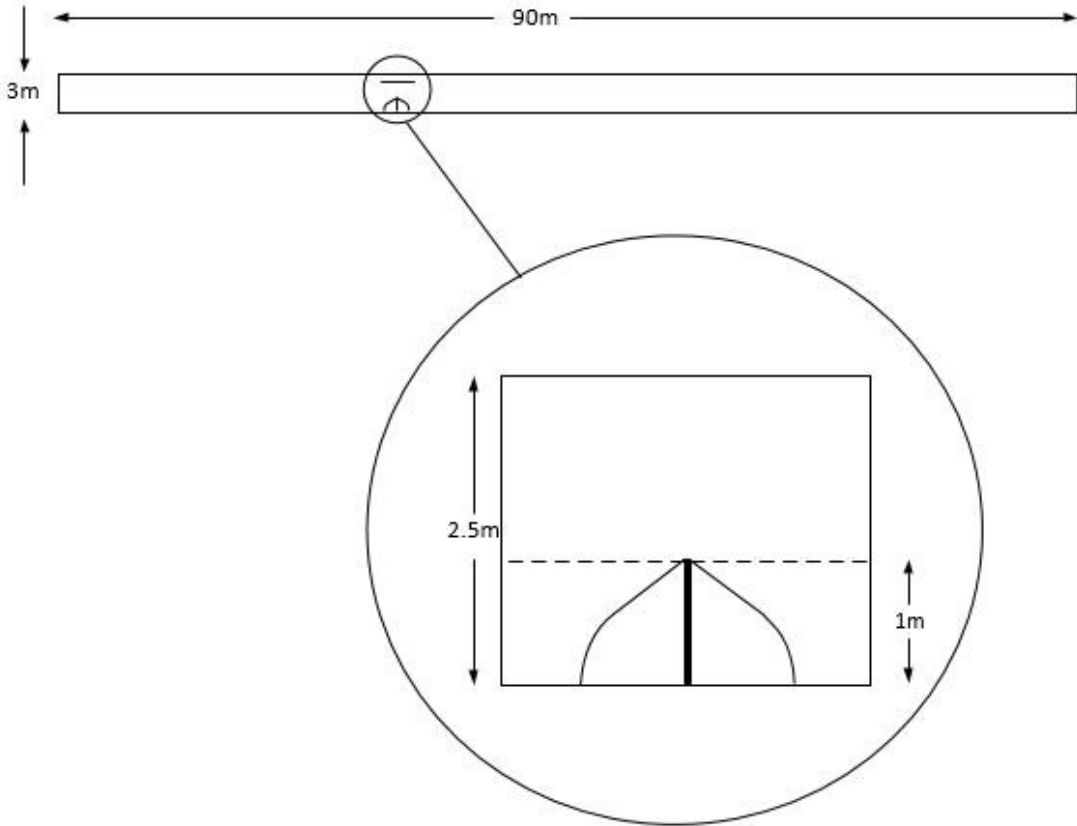
Figure 18: Side view of domain; not to scale
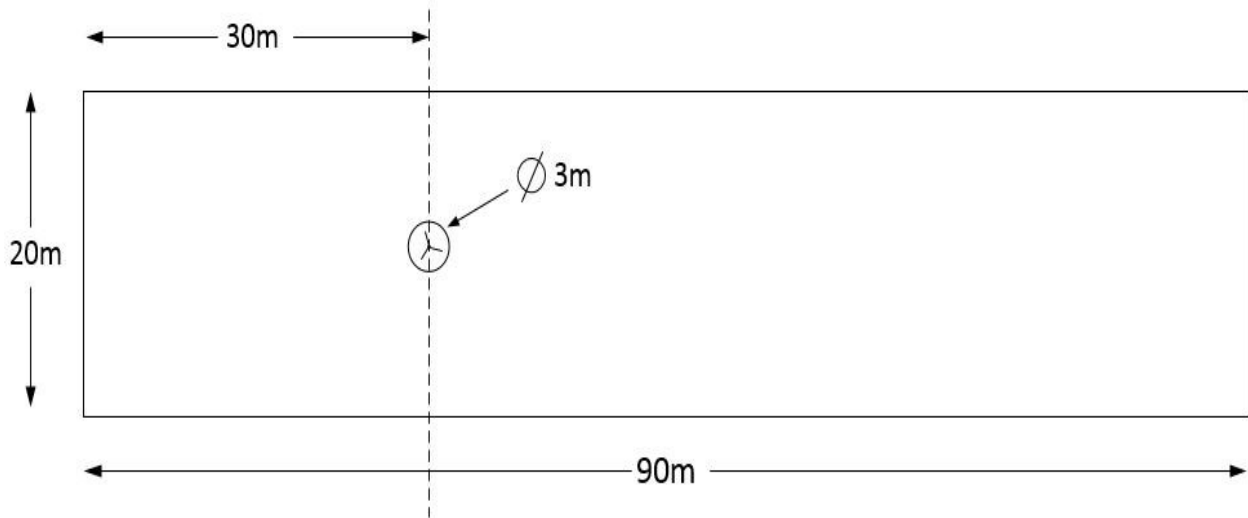
Figure 19: Top View of Domain; not to scale

3.4 Mesh Setup

ANSYS mesher is used to create the mesh over the domain. The division of the computational domain into stationary and rotating domains allows the imposing of different mesh densities. The inflation layer is created around the blade to accurately capture flow separation and to perform reliable simulation of the boundary layer flow. The first layer height is defined by the y^+ condition and the inflation option is used to determine the heights of the inflation layers. The "first layer thickness" is selected to create the constant inflation layers using the value of first layer height. Bedon investigated the extrusion steps and growth rate of mesh, since these parameters influence the total mesh elements. The airfoil edges are split in half to control the number of elements across the airfoil to impose higher mesh density around the leading and trailing edges. A bias factor of 6 is used at the leading edge and bias factor of 3 is applied the trailing edge. Straight cut trailing edge is used and 5 elements of same size are used to capture the geometry. The bias factor is also implied to control mesh density and the uniform formation of inflation layer. There are 223 elements around each airfoil; these elements are swept across the blade surface to ensure better mesh quality and uniform inflation layer. The main characteristics of the mesh are shown in Table 2.

Y+	~1
Number of elements across airfoil	223
Number of elements across blade surface	300
Element size at rotating body interface [mm]	70
Element size at stationary domain interface [mm]	75
Hexahedral cells around each blade	1.6 million
Total no. of elements in rotating domain	4 million
Total mesh count	9 million
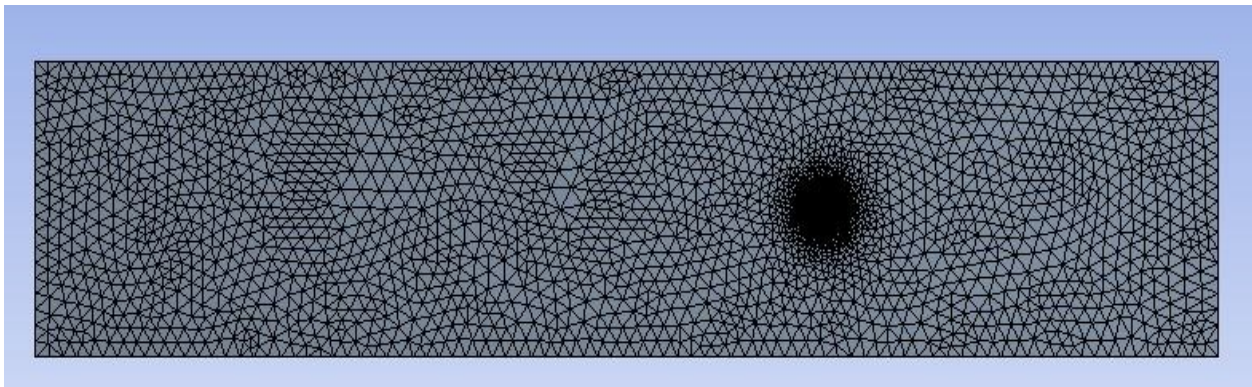
Figure 20: Mesh preview at symmetry plane

The numbers of elements that are swept across the surface are 300, resulting in 1.6 million elements around each blade. A top view of the computational domain is shown in figure 20. Different mesh densities can be observed with bigger elements sizes further from the rotor. Patch independent method is used to create mesh between stationary and rotating domain. This allows control over the maximum element size and lead to a smooth transition of the mesh. The maximum element size in the rotating domain is at the interface, the inflation layer detail and smooth transition of mesh can be seen in figure 21-23. The smooth transition helps to avoid interpolation errors and is defined by the growth rate. Growth rate represent the increase in element edge length with each succeeding layer of elements, the factor of 1.01 is implied, and this results in 1% increase in element edge with each succeeding layer of elements.
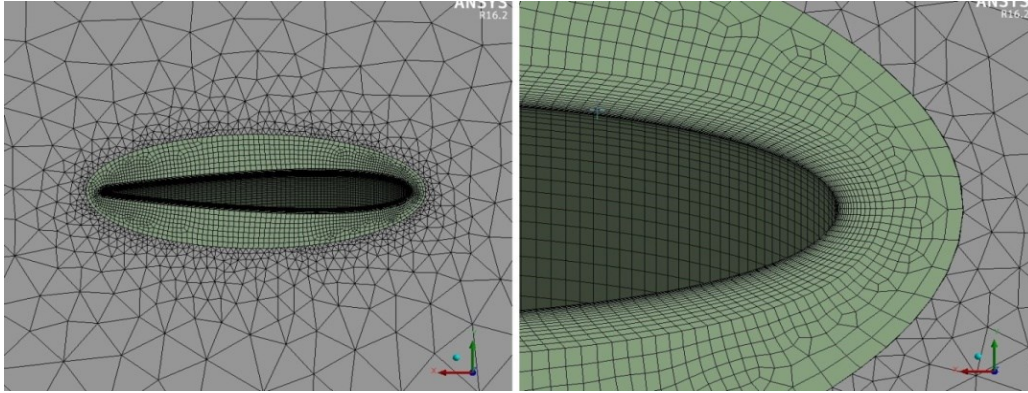
Figure 21: Inflation layers around the blade
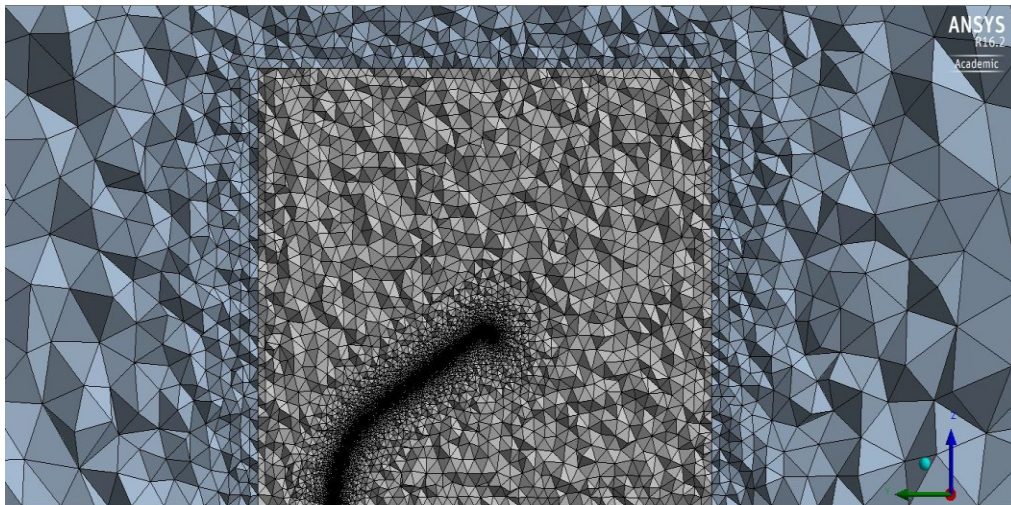
Figure 22: Smooth transition of mesh
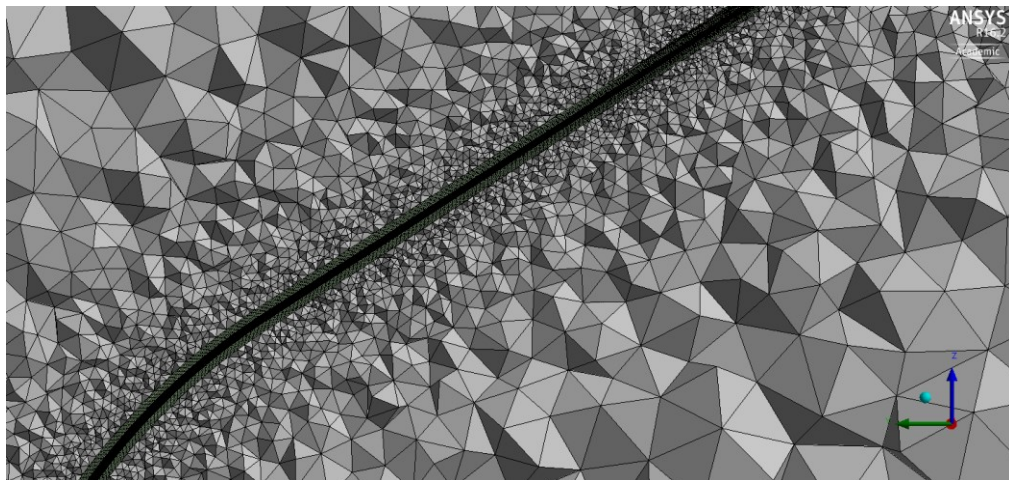
Figure 23: Hexahedral mesh around blades

3.5 Boundary Conditions

Boundary conditions specify the flow variables of the physical model. These are defined as part of the numerical setup of the domain. Velocity Inlet is used at the upstream boundary of the domain with a varying uniform velocity for each case. Symmetry boundary condition is used at the top, bottom and sides. The explanation of boundary conditions is presented in section 2.5. A symmetry boundary condition at the bottom helps to gain advantage of the perfect symmetry of the rotor and computational domain geometry. This helps to reduce computational time and cost. The outlet is considered as pressure outlet with the gauge pressure of 0 Pa. A non-conformal interface is created between mesh refinement region and rotating domain. A similar boundary condition is used between the stationary and rotating domain and a no-slip condition is applied on the blades wall. To reproduce wind tunnel tests, a low level of turbulent intensity 0.1% is set at the inlet and outlet. Turbulent intensity is defined as that ratio between the root mean square of turbulent velocity fluctuations at particular location over specified period of time and the average of the velocity at the same location over same time period. The turbulent viscosity ratio is kept to a default value of 10.
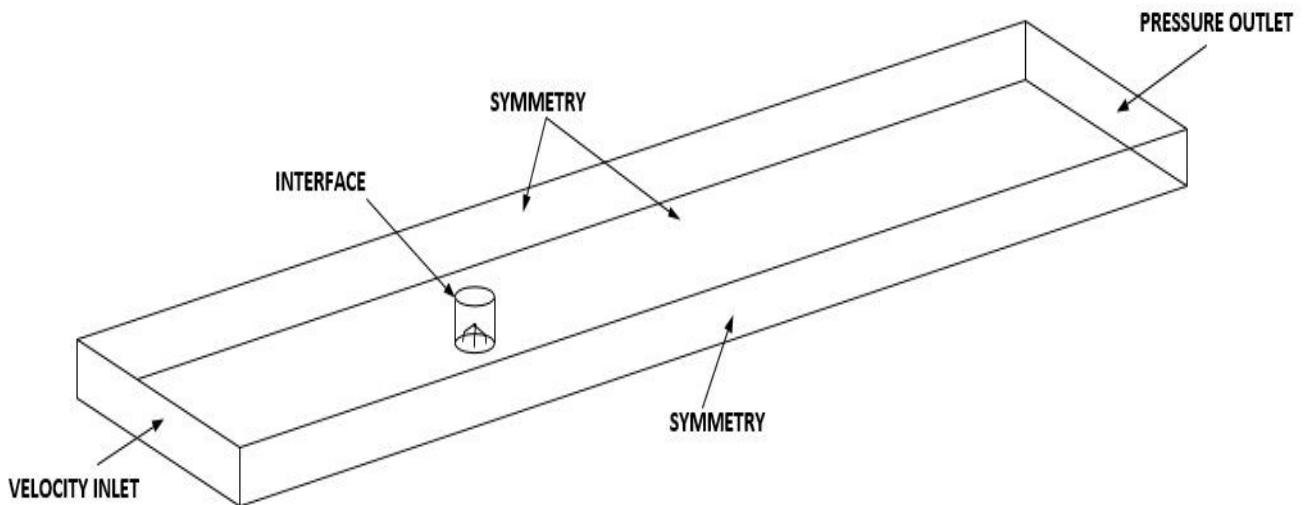
Figure 24: Boundary conditions

3.6 Numerical setup

Transient flow analysis is set up to simulate the transient flow over a specific period of time. Here also the $k - \omega$ SST is used as a turbulence model as proposed by Bedon [35]. The adopted turbulence model is used due to its flexibility in wall boundary treatment. The equations for the model are explained in section 3.1.1. Note that the middle shaft is not included to reduce the complexity of the problem and to avoid meshing issues at the blades joint. Air with a density of 1.225 kg/m^3 and dynamic viscosity of 1.7894.10^{-5} kg/m.s is selected as fluid. The mesh interface is created around the refining zone and rotating domain, also between rotating and stationary domain. The sliding mesh technique is employed at all non-conformal interfaces, this allows the nodes to move rigidly in the given dynamics mesh zone. As the mesh motion is updated in time the non-conformal interfaces are likewise updated to reflect the new positions at each zone. The major difference between dynamic and sliding motion is that all the cells retain their original shape and volume and slide along the interface boundary. All three cases are performed considering only one rotational speed of 400 rpm with varying inlet wind speed. The inlet wind speeds are calculated using eq. 1.

The SIMPLE (Semi –Implicit Method for the Pressure Linked Equations) algorithm is used for the pressure velocity coupling. It is a segregated scheme that solves the pressure and velocity fields separately; the details of the scheme are presented in section 2.7.1. The default least cell square based gradient is used for gradient evaluation. Gradients required for values at cell faces, secondary diffusion term and velocity derivatives are calculated using this method. Second order upwind scheme is used for momentum, pressure and turbulent dissipation rate.

The second order implicit is selected for the temporal formulation, although second order implicit scheme is computationally expensive and takes longer to converge. The time step size is equal to the time needed for the rotor to perform an azimuthal rotation of 1 degree. The moment of coefficients (C_m) for the blades is obtained as an output from FLUENT. The final value of the moment is calculated for one rotational cycle, when coefficient of moment reaches repeatable oscillatory behavior. The simulation is considered as periodic when the average output values does not vary more than 1%, and the step is considered converged when the residual value falls below 10^{-5}.

3.7 Validation results and discussion

Results obtained are calculated for different tip speed ratios for varying the inlet wind speeds. The moment of coefficients (C_m) for the blade is obtained as an output from FLUENT and is set as the monitor for solution convergence. It is computed and stored at the end of every time step. The values computed are dependent on the reference area of the rotor given at numerical setup and the initialization of the solution is based on the inlet condition. The torque variation for TSR 4 is shown in fig 25.

Three corresponding TSR values of peak power coefficient are selected for validation. The power coefficient is calculated using eq.2. Bedon conducted the boundary layer extrusion studies and concluded that 27 step mesh extrusion with growth rate of 1.15 is closer to experimental results compared to 15 step layer of different growth rate. It was also reported that 27 steps extrusion cannot be used for full turbine study due to memory limitations. The results for 27 steps are compared with CFD results and shown in figure 28. The solution converges after 2500 time steps, which corresponds to approximately 7 cycles.
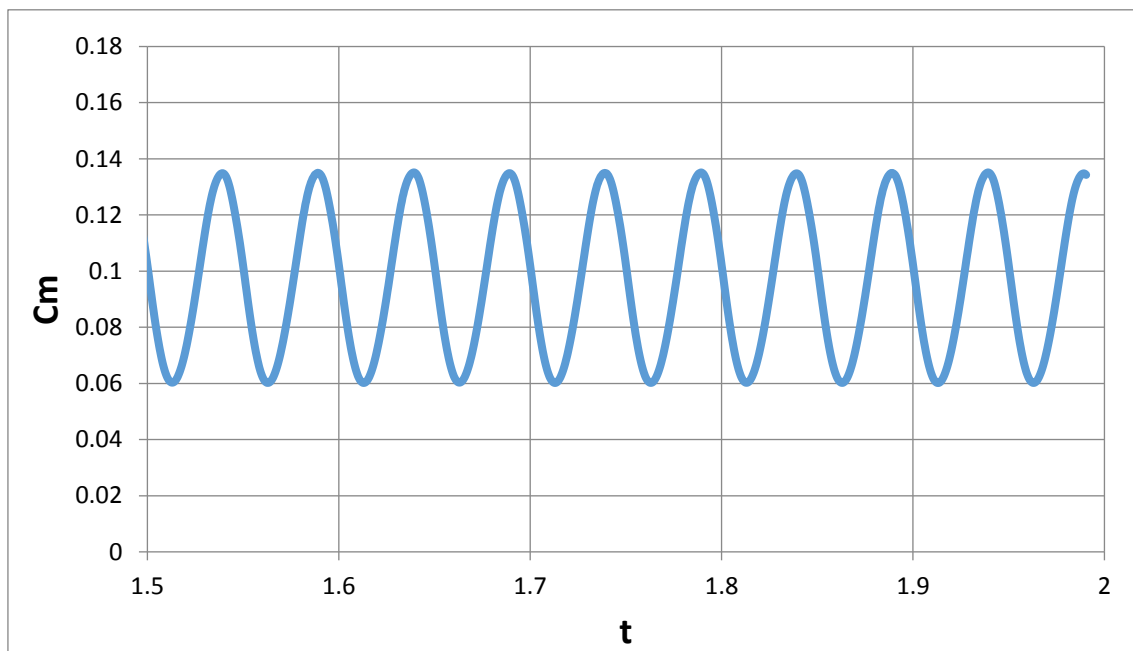
Figure 25: Moment Convergence graph for $\lambda = 4$
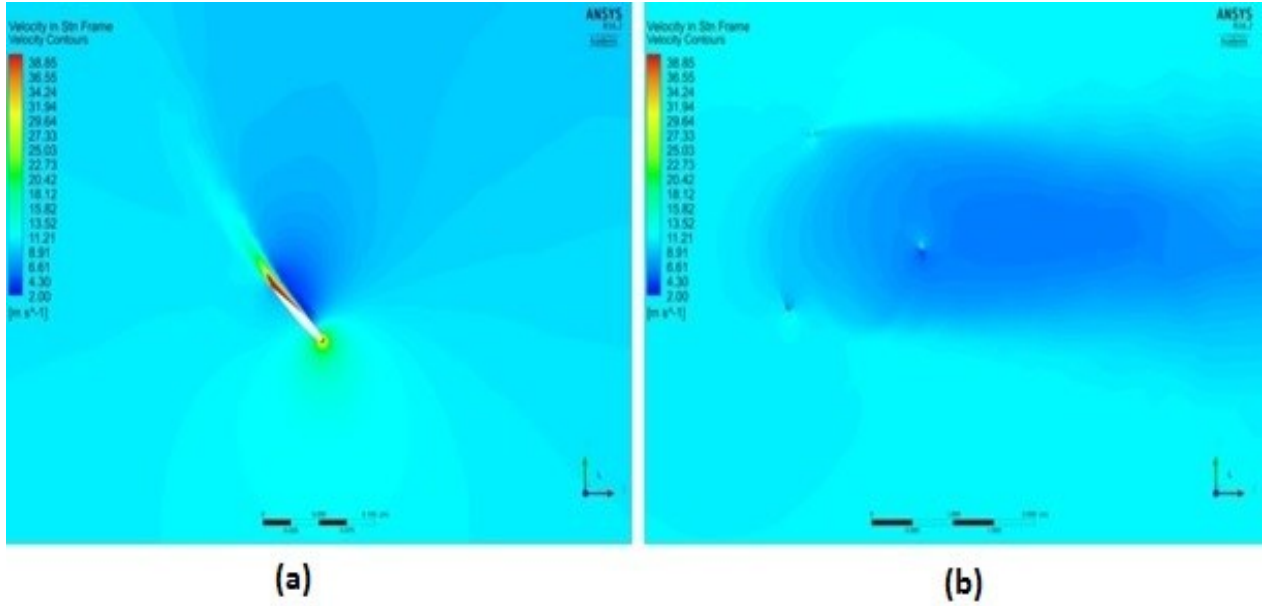
Figure 26: Velocity contours (λ = 4) (b) Wake behind the rotor (top view)
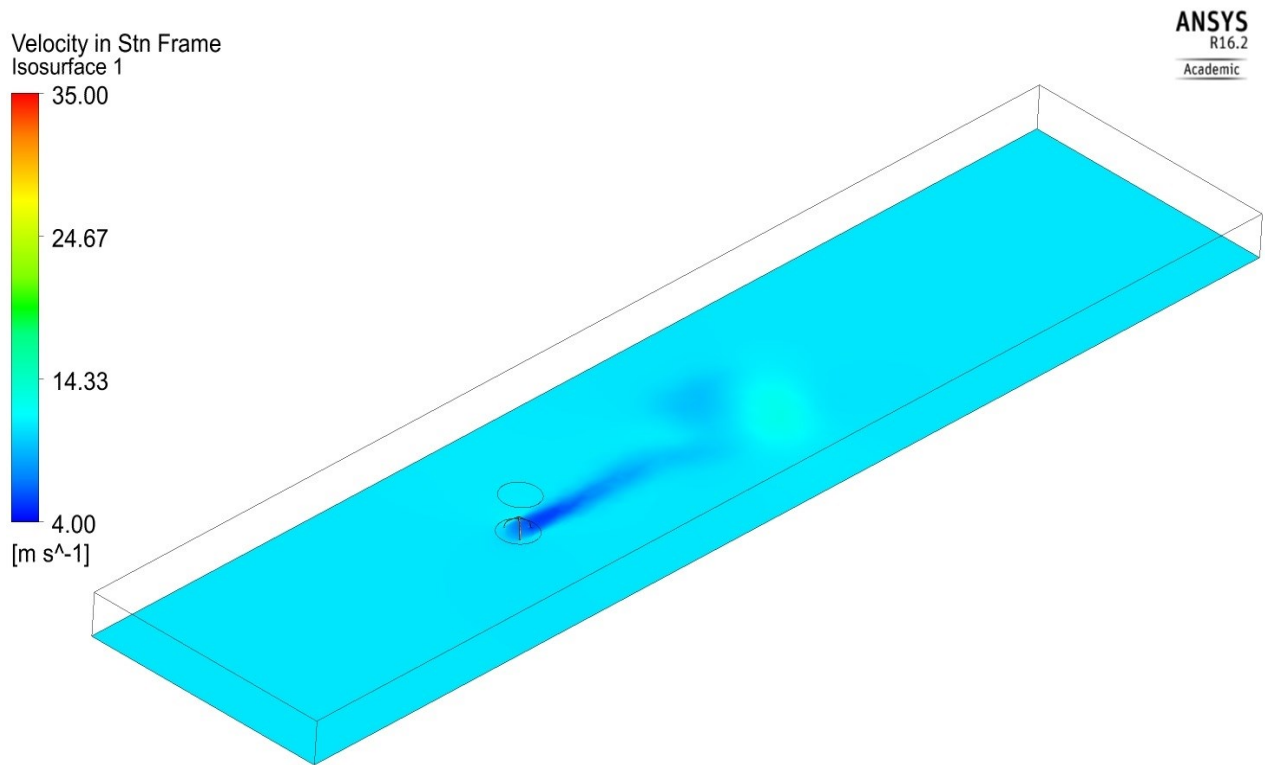
Figure 27: Wake produced behind the rotor (λ = 4)
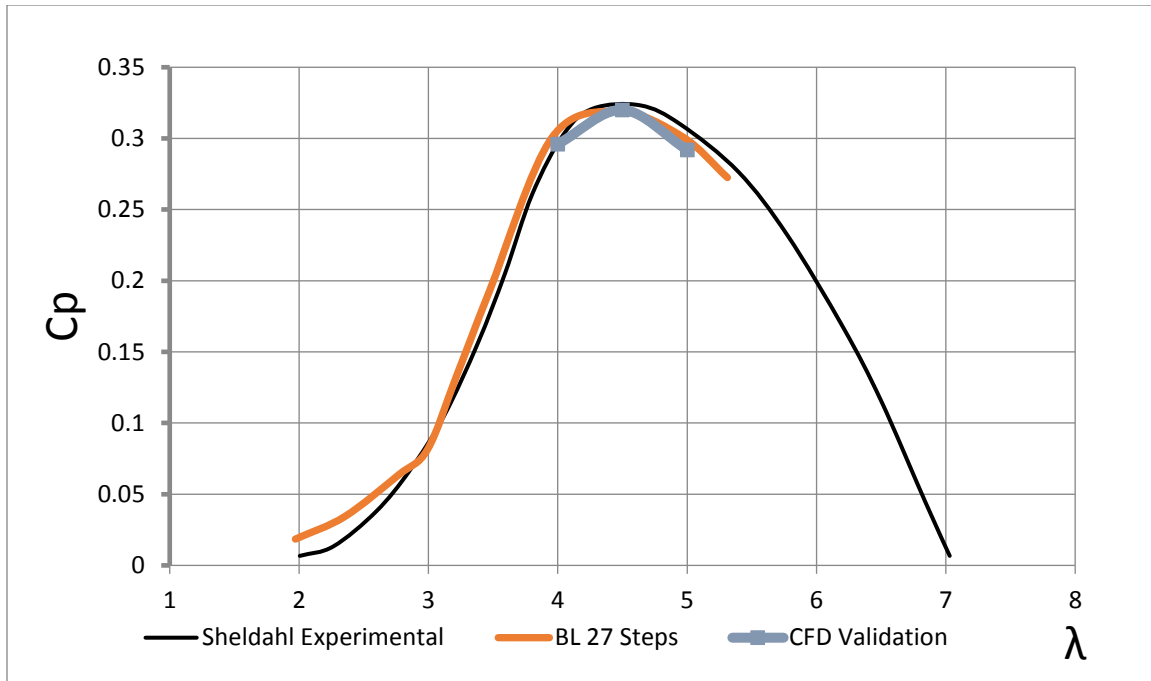
Figure 28: Power Coefficient VS. Tip speed ratio curve Comparison

Fig. 26 (a) shows magnification of velocity contours on a single blade. It shows the high velocity at the trailing edge of the blade. Fig. 26 (b) shows the velocity contours (after 7 cycles) from top view at the plane where symmetry boundary condition is applied for the rotor. The aerodynamic wake effect is shown in 3D at the symmetry plane. Fig. 27 shows a large wake of slower and more turbulent air is produced behind the rotor. This can be helpful in solving wind farm optimization problems.

Fig. 28 shows the CFD validation against the experimental results by Sheldahl and CFD results by Bedon for 27 boundary layers. The coefficient of power calculated for different inlet wind speeds, shows good agreement with the values. The experimental and CFD curves follow similar trend, hence validate the meshing methodology (number of inflation layers, element size at interfaces), Numerical setup (time step size calculation, spatial and temporal discretization schemes, turbulence model). The curves shows increasing trend for Tip speed ratio $2 - 4.5$. After this value, the curves decline with the increase in TSR. The number of convergence cycle is approximately same for all the cases and maximum value of power coefficient is observed at $\lambda = 4.5$.

CHAPTER 4: ROOF MOUNTED VAWT TROPOSKIEN

Increasing greenhouse emissions and global warming scales has led to increasing significance of the renewable energy. The exponential growth of wind energy will likely to expand at a brisk rate. The increased interest to exploit building roof tops area for renewable energy installation is observed; this includes photovoltaic, solar thermal systems and small scale wind turbines. Building integrated-mounted wind turbine (BUWT) is the generic term used to define any wind turbine that can be incorporated within the built environment [42]. The high rise buildings are most suitable among all building types, due to maximum potential for high wind flows. These building augmented wind turbines can effectively be exploited to provide delocalized power in the built environment. This means that the produced energy can be fed directly to the grid of the building thus reducing transmission losses.

The micro wind turbines are defined as the wind turbines with capacity less than 2.5 KW [43]. However, the American wind energy association defines "small scale" as less than 100 KW, but size can vary according to needs and laws of the country or state. The roof shape is identified as important factor on the performance of the turbine, therefore cube shaped; flat roof building is used for micro-wind turbine analysis. The CFD study for micro wind turbine roof mounting site analysis was performed by Ledo [44]. Wind flow simulation for different roof profiles were performed with three different roof profiles, pitched roof, pyramidal roof and flat roof. It was concluded turbulent intensity strongly depends on the roof profile as well as wind directions. The wind over flat roofs experienced lower turbulence intensity compared to other roof profiles and turbulence beyond the roof decreases rapidly. There is an increase in wind speed on all roof types compared to the free stream velocity. Compared to other roof profiles, flat roof profile shows consistent higher speeds at the upstream edge of the building except for the region in the proximity of the upstream edge where flow is separated.

Wind direction and variability are important consideration for turbine placement. Paul Blackmore asserted that wrong placement of turbine can lead to zero power output for significant periods of time, even when the wind is blowing strongly [45]. Another factor for the cautious integration of building mounted wind turbines are liability, vibration, physical damage, wakes, bird strikes, noise pollution, inadequate energy production, economic potential of urban wind

turbines and NIMBY (Not in my backyard issues). The site monitoring study done by Massachusetts CADMUS group on the potential causes for the underperformance of building mounted wind turbines found that urban site conditions that reduce the wind speed are not the sole reason for the low energy production. The accuracy of manufacturers, power curves, losses from balance of system components and losses from additional site conditions (close obstacles causing turbulence and wind shear) have also been identified as major losses [46].

The technical challenges include the uncertain productivity at different wind speeds in close proximity of the upstream edge. The random patterns of productions can yield risk of wear and tear, which could lead to reduced life time of the system, safety concern and deteriorated performance of the turbines. Among different available options, Darrieus Wind Turbines are being considered a more appealing choice due to their low visual impact, the reduced acoustic emission and their better response to turbulent and skewed oncoming flow [47]. The numerical and experimental study of vertical axis wind turbines is widely studied in literature. The primary focus of study for Darrieus wind turbines is aerodynamic performance analysis and geometric modifications to increase the lift to drag ratio. On the other hand, the purpose of roof mounted wind turbine is easily understood as the small rotors on rooftop can exploit higher zone of wind profile. The onsite power generation can help to fulfill the requirements of the sustainable design of a new building. An array of these turbines can be installed on the roof as vertical axis wind turbines needs distance of six times of their rotor size to recover 95% of wind velocity lost in wake in downstream distance [48]. On the other hand, the velocity recovery zone for horizontal axis wind turbine is much higher. Turbines in wind parks are spaced somewhere between 5 and 9 rotor diameter apart in the prevailing wind direction and between 3 and 5 rotors diameter apart in the crosswind direction. The details of optimal Vertical axis wind turbines placement study is discussed in chapter 1.5. It is seen in section 2.2 that wind conditions at the upstream edge of the building leads to flow acceleration. This forms the basis of this study to investigate and understand the optimal placement position of the turbine.

4.1 Turbine Geometry and Computational Domain

The large oscillatory conditions on the Vertical Axis Wind Turbines blades can lead to fatigue failure. The development of "skipping rope" or Troposkien shape was done to improve fatigue design and analysis technique for increased turbine longevity [10]. Back in 1970's, the National Research Council of Canada observed that under the action of centrifugal forces, a perfectly flexible blade assumes the approximate shape of catenary. The assumed catenary shape looks like a perfect flexible cable of uniform density and cross section hanging freely from two points. Once the cable rotates at the constant velocity, it deviates from the catenary and becomes a "Troposkien".

The assumption of perfect symmetry between the top and bottom part of the rotor is not valid for roof mounted wind turbine analysis, therefore full scale 3D model is used. ANSYS Design Modeler application is used to model the 3D turbine geometry as shown in figure 29. The application is known for its ability to transform 2D sketches of lines, arc and splines into 3D models. Similar to the validation part, the NACA 0012 profile is used for blade profile. The airfoil is formed from the imported coordinates and swept across the blade profile. A Boolean-Subtract feature is used to distinguish stationary and rotating part of the computational domain. The approach helps to apply different mesh densities and interface boundary condition.
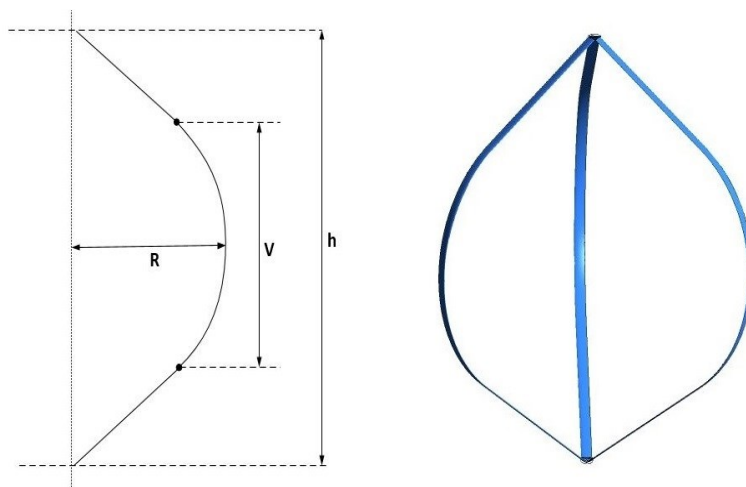
Figure 29: Geometry details of full turbine

The geometrical specifications of the turbine are derived from the tested model used by Sheldahl for wind tunnel tests [11]. He used conventional test procedures methods, the turbine was rotated at a rotational speed, which was determined and controlled by speed controller. The wind velocity was adjusted to predetermined value and steady state torque was measured. The procedure was repeated with new wind speeds until sufficient data points are obtained to define the performance of the turbine. Likewise, the similar strategy is used for this study, the inlet wind speeds are varied, while rotational speed is kept the same. The main geometrical specifications are reported in Table 1.
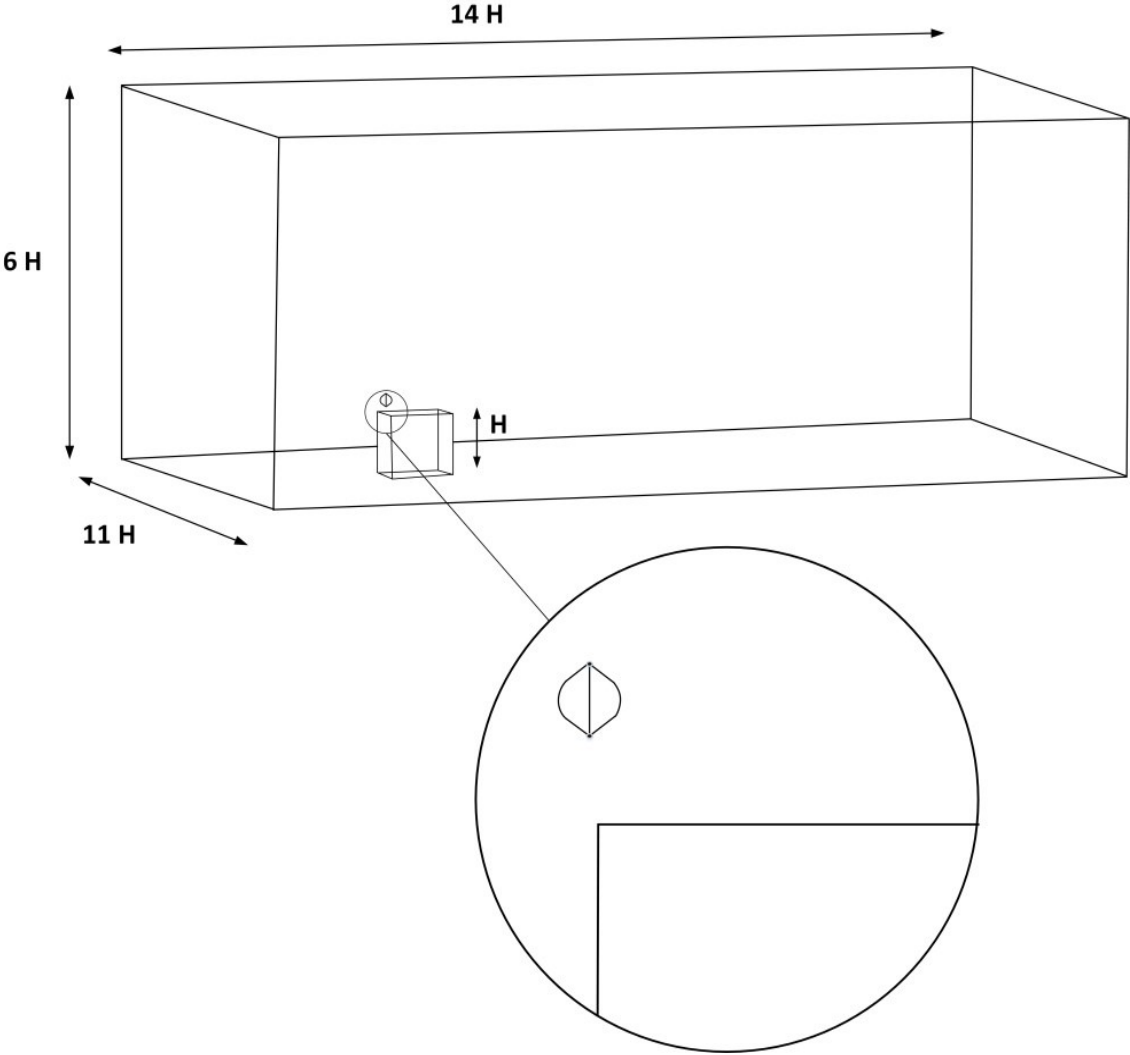
Figure 30: Isometric view of domain

The CFD analysis for different roof profiles is thoroughly discussed by Ledo [44]. It was concluded in the study that flat roof profiles lead to lower turbulence intensity and rapid decrease of turbulence compared to other roof designs. Fig. 30 shows the isometric view of the computational domain and cube shape of the building having same dimension of length, width and height. The dimensions are normalized as a function of the building height "H" as suggested by Tominaga [49]. For the single-building model, the lateral and top boundary should be set at 5H or more from the edge of the building. The inlet is places 3H from the upstream edge of the building and the outflow boundary is suggested at 10H behind the building to avoid reverse flow. Figure 31 shows turbine placement positions and front view of the domain. The dimensional distance of three dots from the upstream edge is magnified and normalized as function of rotor's height (2 m). Turbine sits on the top of each dot and wind gradient is imposed at the inlet boundary with desired velocity pointing at the middle of the rotor. The details are discussed in numerical setup of domain.
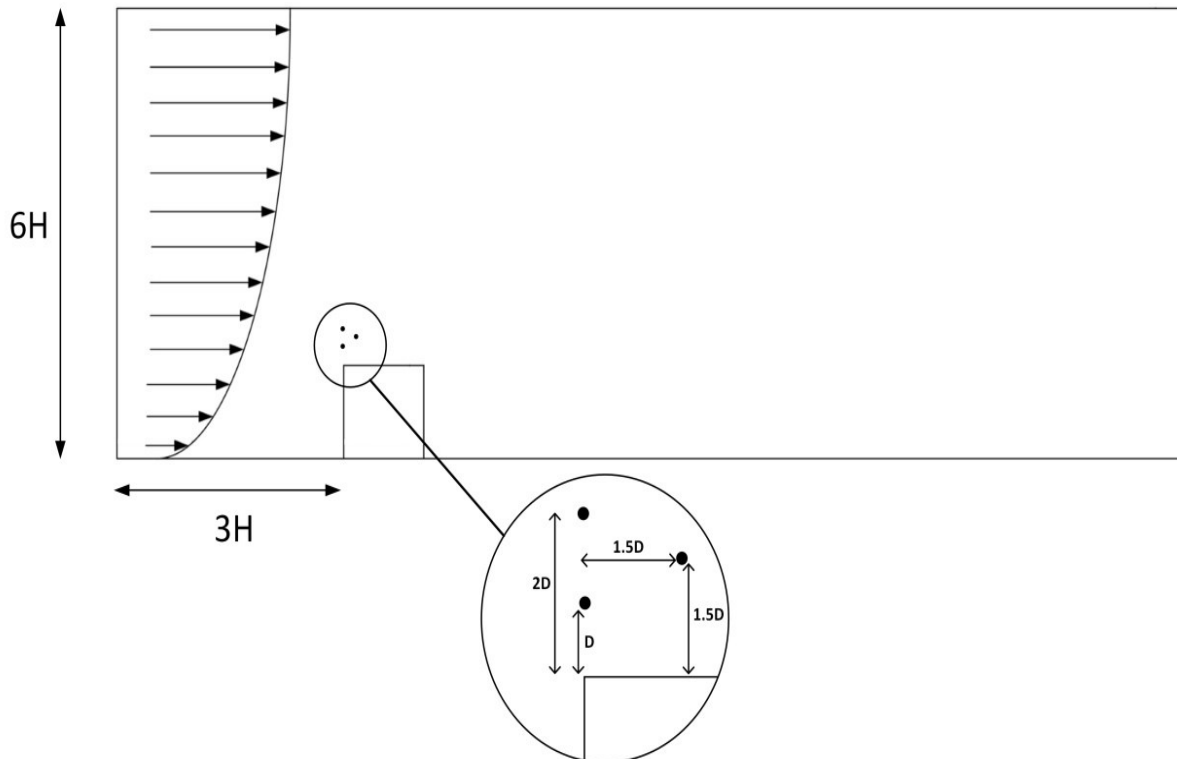
Figure 31: Front view of domain and Turbine placement positions

43

Three different turbine placement positions at different heights are investigated, to study the optimum power coefficient output at different tip speed ratios. It is expected that a suitable position of turbine will help to increase the coefficient of power (than the baseline value of 0.33) as the velocity flow acceleration from the upstream edge could be 29% greater than free stream velocity [25]. The maximum wind speed location at the upstream edge is chosen for the turbine placement. Selected locations heights are made a function of rotor's diameter. The dimensions are important to avoid small wind velocities and large turbulence close to the separation bubble. The three dimensional CFD analysis for the wind speed on rooftop was performed by Martens [26]. ABL was used to simulate the flow around a building of height 20m. It was suggested that, if Δh is the certain placement height of the turbine and h is the height of the building, then turbine placement height should be $\Delta h/h \geq 0.05$ for the edge position and $\Delta h/h \geq 0.25$ for the center placement position to avoid high turbulence of big contours on the rooftop.
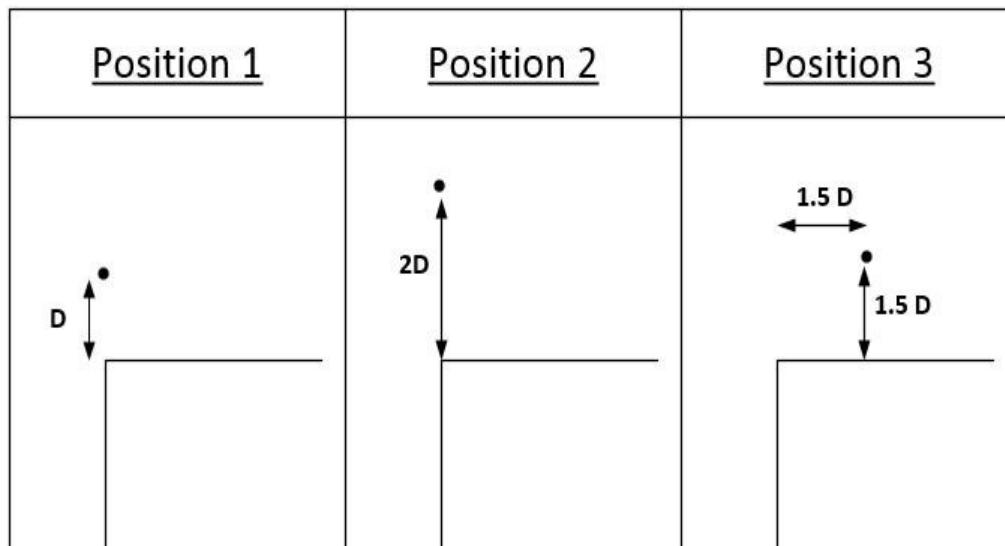
Figure 32: Details of Turbine placement

4.2 Mesh setup

ANSYS workbench mesher is used to generate the mesh of computational domain with physics and solver preference set to CFD and FLUENT respectively. The Boolean operation executed at the CAD modeling design phase helps to apply part-based meshing methods. The mesher operates one part at a time and enables patch independent meshing technique for every face and boundary of the domain. Both, local and global mesh controls are assigned to dictate mesh refinement zones, faces and edges. The advanced size function is set to on and refinement is set to proximity and curvature. This provides additional control on the mesh domain to define the minimum and maximum size of element, growth rate, curvature normal angles and smoothing of elements. The relevance center is set to "medium" to have reasonable refinement for the entire model. This option has a trade-off between the accuracy and total number of elements in the domain as default "coarse" relevance center option has least accuracy. The smooth transition is defined by growth rate and is recommended for bodies with sweepable inflation. The function achieves smooth transition of elements growing away from the boundary cap and improves overall quality of the mesh by moving location of nodes with respect to surrounding nodes. Slow transition is used to control the growth rate of elements. Patch independent tetrahedron method with proximity and curvature refinement is also defined for the rotating and stationary domain. The growth rate of elements is decreased to 1.01 for the rotating region and 1.15 for stationary domain from default value. The value for number of cells across the gap is increased to 6 from the default value of 3 to set target for narrow gaps. The mesh will subdivide in tight region towards the prescribed value and will help to have better refinement in area between the maximum radius of rotor blade and rotating domain interface.

Hybrid mesh technique is used to create mesh over the domain, this helps to fill a given volume more efficiently than other mesh shapes. The hexahedron meshes are more uniform and can be more accurate when align with the flow direction. Airfoil edges are split from the middle to apply smaller element size at the leading and trailing edges. A bias factor with hard behavior is used to perform the desired operation. Bias factor is defined as the ratio of largest edge to the smallest edge and setting the behavior to hard gives priority to the bias setting in mesh formation. 132 elements with bias factor of 5 are defined for the leading edge, 88 elements in total with bias factor of 3.5 are applied to the upper and lower part of the trailing edges and 4

elements are defined in the small closing edge of airfoil. The curvature normal angle is set to 12 degrees, it restricts the maximum allowable angle that one element is allowed to span. The defeaturing tolerance option is also enabled to defeature small features and dirty geometry. A hexahedral mesh is created over the blades from quadrilateral elements that are swept across the blade surface along with the inflation layer. The first layer height is defined by Y+ conditions using eq. 4, it generates thin element layer adjacent to the boundary to efficiently resolve the boundary layer. The sweep method control command allows sweep mesh on a "sweepable body" on topology consistent source and target faces. Hex dominant mesh method is enforced in sweep elements by selecting all quad method under free face mesh type. The total numbers of 640 elements are specified through the sweep direction. The number of elements around the airfoil is kept to 224, since this parameter strongly influence the total number of mesh element count. The sweeping source and targets planes are manually chosen to ensure the sweep and inflation across the blade surface. The main parameters and advance size function setup of mesh are listed in Table 3. Figure 33 - 34 shows the sectional view of the domain; it gives idea about the refinement zones and total number of elements in domain.

Table 3: Main parameters of the mesh

Y+	~1
Number of elements across airfoil	224
Number of elements across blade surface	640
Element size at rotating body interface [mm]	145
Element size at stationary domain interface [mm]	130
Element size at roof top and front wall of the building [mm]	230
Hexahedral cells around each blade	3.3 million
Total no. of elements in rotating domain	14 million
Total mesh count	28.4 million
Summary of Advanced Sizing Functions	
Minimum size [mm]	0.01
Proximity Min. size [mm]	0.005
Maximum Face size [mm]	5000
Maximum size [mm]	5500
Growth rate	1.2
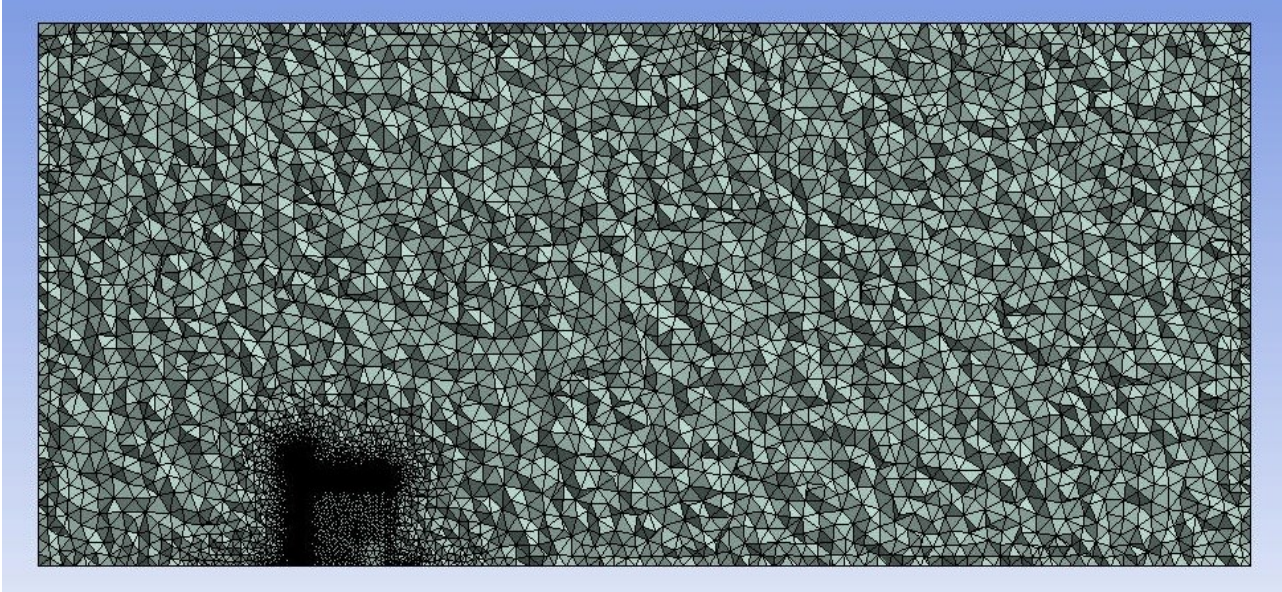
Figure 33: Sectioned view of domain
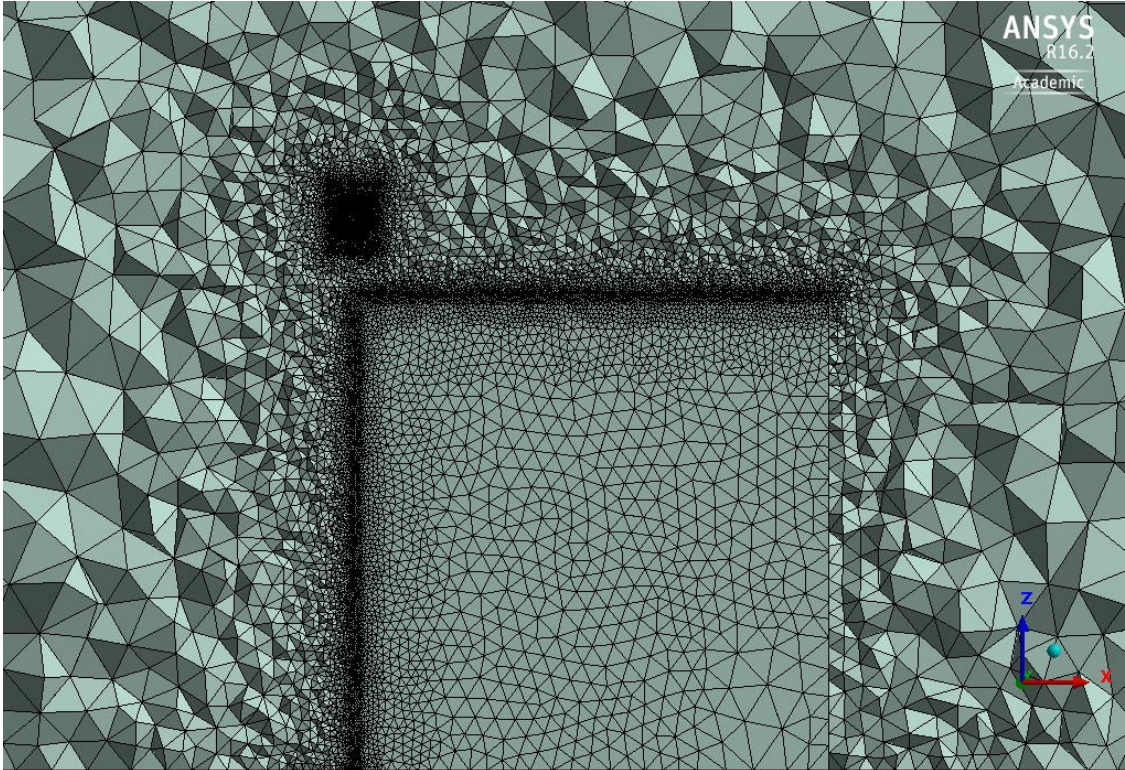
Figure 34: Mesh Refinement on the Interfaces, Upstream edge & roof of a building
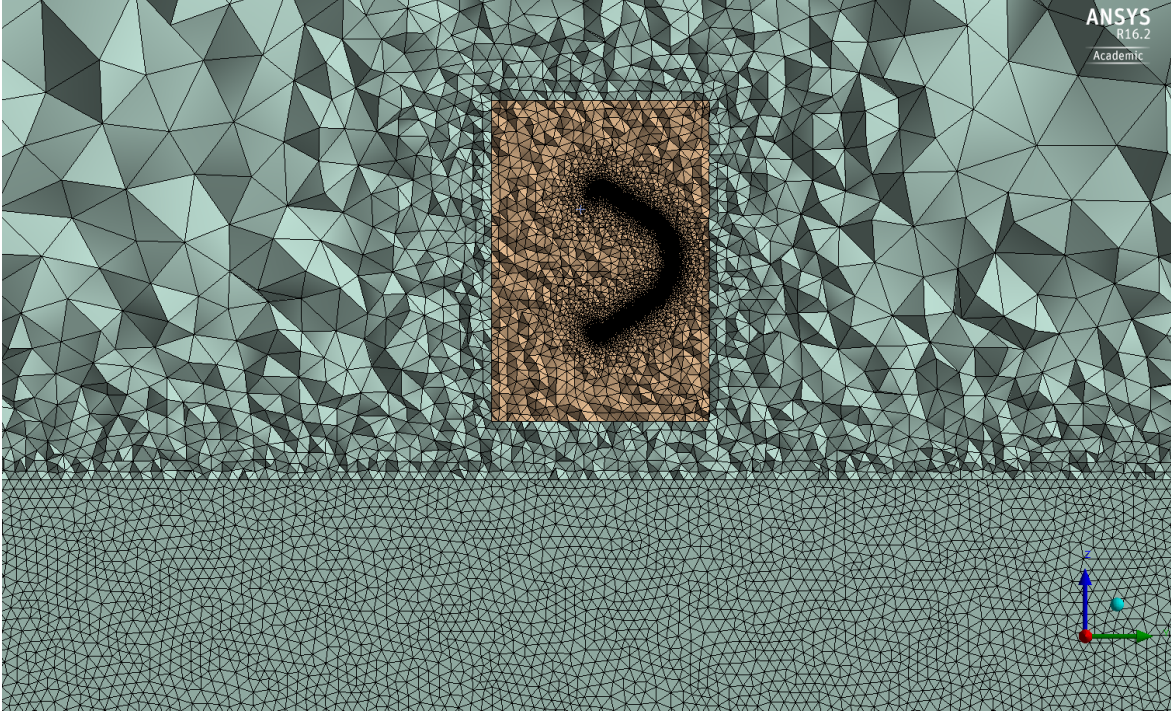
Figure 35: Mesh refinement around blades and on rooftop
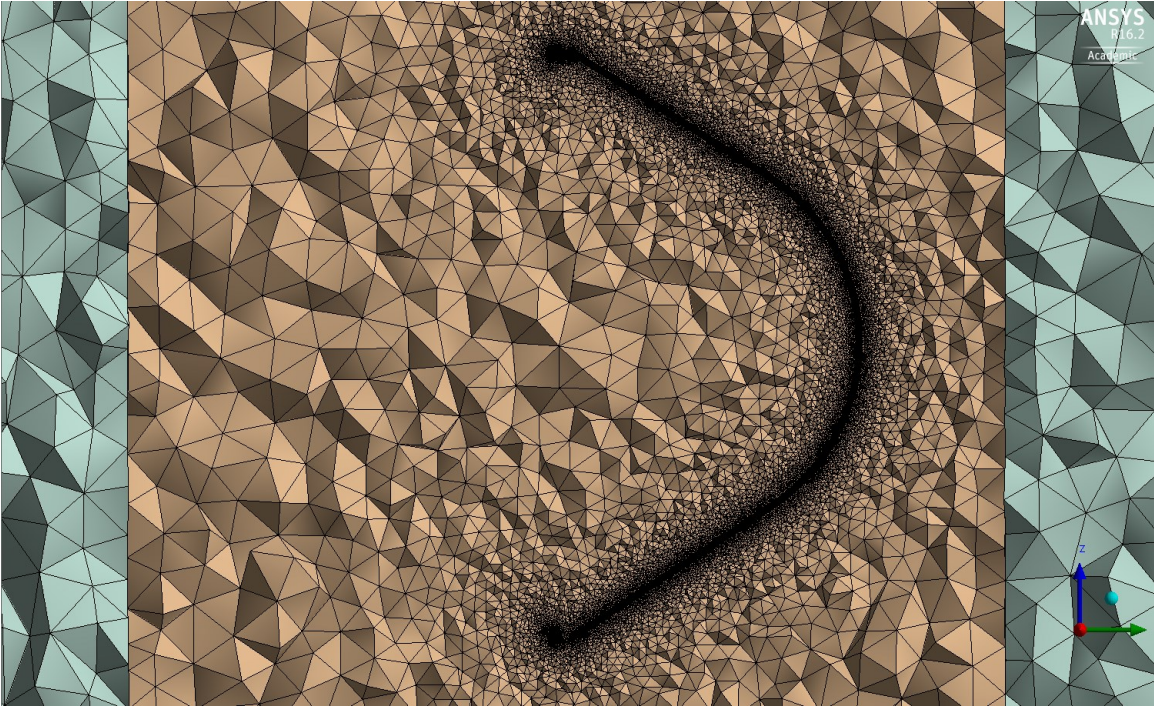
Figure 36: Hybrid mesh and smooth transition
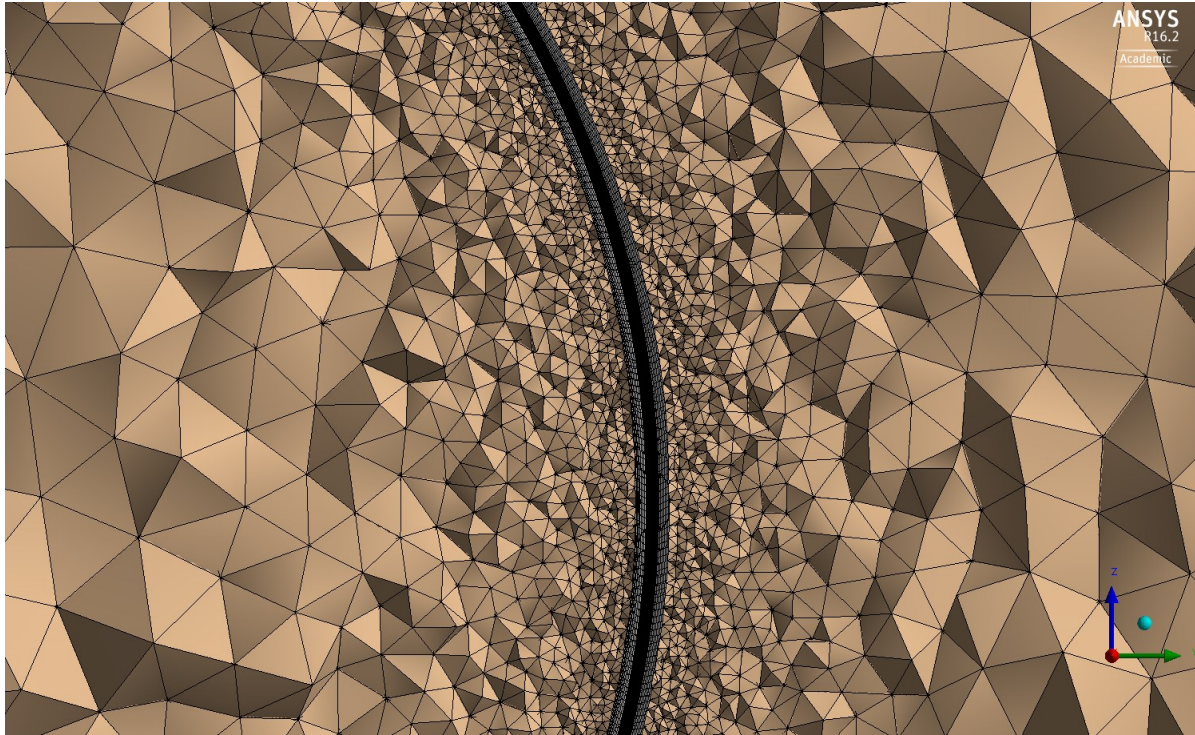
Figure 37: Hexahedral mesh around blades

Fig. 35 shows the sectioned view of the domain and shows the mesh refinement around the blades, rotating domain interfaces and upstream face of the building. Small mesh elements are seen around the blade, the hybrid mesh characteristics and smooth transition of mesh is further magnified in figure 36 and figure 37. The roof top is also refined to accurately capture the vortices as separation bubble is formed on the rooftop after boundary layer separation. It also helps to capture vortices formed around the building and flow acceleration zone in proximity of the upstream edge. Non-conformal meshing technique is implied at the interfaces, this permits the cell zone to be easily connected to each other by passing fluxes from one mesh to another. The aspect ratio of elements at the leading and trailing edge is "5" and "9" respectively. The Skewness is the primary quality measure of the mesh, the maximum skewness of entire mesh is 0.86 with an average value of 0.27. Higher value of skewness factor is reasonable for complex geometry and bigger mesh sizes. The value greater than 0.9 is not desirable and can lead to divergence or misleading results as the equations being solved assume that the cells are relatively equilateral.

4.3 Boundary Conditions
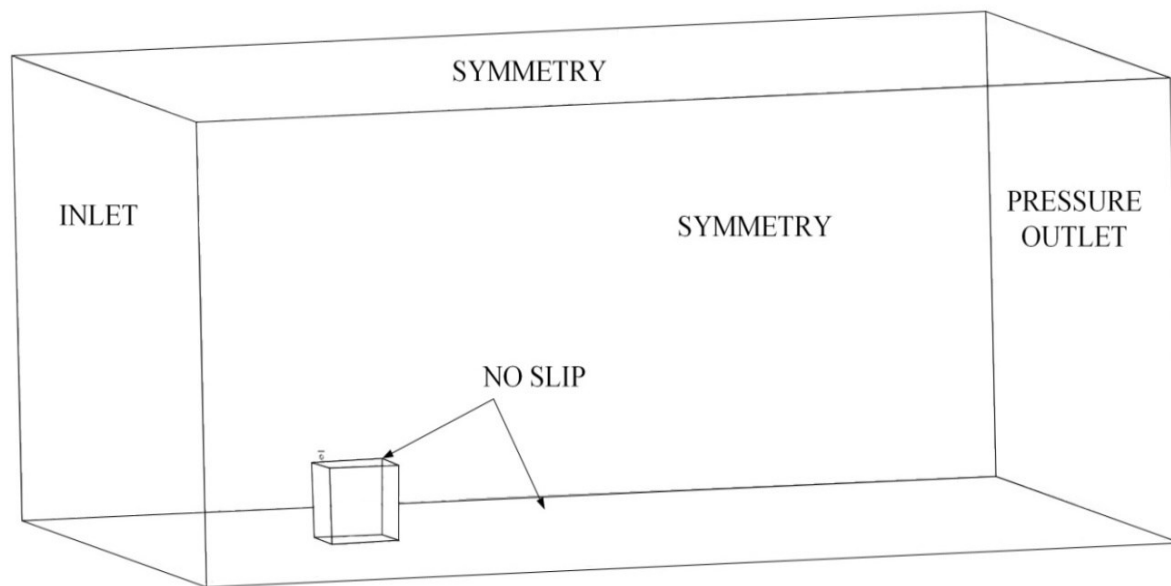
Figure 38: Boundary conditions setup

Fig 38 shows the boundary condition setup of the computational domain; no-slip condition is applied at all faces of the blades, ground and walls of the building. This defines shear condition at the wall surfaces and indicates that fluid sticks and moves with the same velocity as the wall. The non-conformal interface is created between the stationary and rotating domains and also between the mesh refinement zone and rotating domain. The wind gradient is imposed at the inlet in the positive x-direction and is defined by eq.3. The desired velocity is set at mid rotor height. The symmetry boundary condition is applied at the sides and top of the domain. The symmetry boundary condition is normally used, when physical geometry and flow pattern have mirror symmetry but in this case it represents the zero-shear slips on the walls. In other words, velocity value normal to the surface is considered zero. Pressure outlet is imposed at the outlet boundary with gauge pressure of 0 Pa.

4.4 Numerical setup

Turbulence modeling is required to model unsteady behavior of transported quantities in time and space. Transient analysis is time periodic solution in which the flow values fluctuate with repeating pattern. Density based coupled solver takes pressure and momentum as primary variables. Parallel processing approach is used for large mesh which allows FLUENT to run on multiple processors to decrease computational time. This method allows the solver to divide mesh on all the assigned processors by a partitioning method. For non-conformal meshes, the default technique of principal axis is changed to metis. The metis is also called bi-section algorithm and used a multilevel approach. The method approaches in steps, the solver bisects the entire domain into equal subdomains and repeat the process for desired bisection level. The two equation model K-omega SST is selected as the turbulence model and air with a density of 1.225 kg/m^3 and dynamic viscosity of 1.7894.10^{-5} kg/m.s is selected as fluid**.**

The transient effect due to flow interaction between the stationary and rotating domain requires the Sliding Mesh Method. It is a special case of the dynamic mesh motion, wherein nodes move rigidly in the dynamic mesh zone, provided that cell zone are connected to through non-conformal interfaces. The non-conformal mesh boundary should remain in contact to continuously slide along the interface boundary. It is required to update new positions of non-conformal interfaces. The method is able to define the motion of rotating domain about the fixed axis and motion of the blades relative to rotating domain. The rotational velocity of the rotating domain is 400 rpm for each case, whereas sliding mesh technique is used to interpolate between the rotating and stationary domain. Moving wall option is selected for all blades. The refinement zones for each blade are identified by the solver under adjacent cell zone. The blades are given wall condition with no-slip shear condition and are specified along the z-direction. The wall boundary conditions of domain are explained in section 4.3. Moment coefficient is set as output for all three blades and the values are obtained relative to the stationary domain. The solution initialization and the moment coefficient output are based on the condition set for inlet conditions. A turbine is placed on the top of each dot with desired velocity at the middle of the rotor. Wind profile is imposed at the inlet boundary in the positive x-direction. For each case, the desired velocity points at the middle of the rotor as shown in Fig. 39. The formulation of the ABL is given by Eq. 3
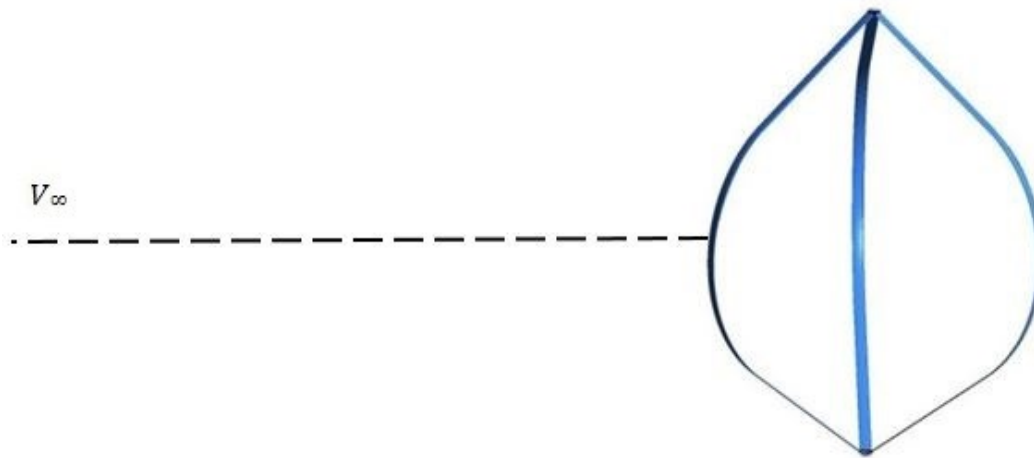
Figure 39: Desired Velocity at mid-rotor

The SIMPLE scheme is used for pressure velocity coupling and the algorithm is derived by reformatting the continuity equation. The detail of the scheme is presented in chapter 2.7.1. Least square cell based technique is used for gradient formulation. The gradients are used to compute the secondary diffusion terms and velocity formulation. The spatial discretization is performed considering second order schemes. Standard scheme is used for pressure interpolation. It interpolates the pressure values at the faces using momentum equation coefficients. Temporal discretization involves the integration of every term in the differential equations over the time step Δt. A first order implicit scheme is used for temporal discretization and under relaxation factors are left as default. The time step size for this case is based on the number of steps per rotation. To reduce the computational time for large mesh, time step size of 1 degree is used. This corresponds to 360 time steps per rotation. The simulations are performed for a range of tip speed ratios. The inlet wind velocity varies, while the rotational speed is fixed at 400 rpm for each case. The flow over the surface produces an increasing pressure distribution along the flow direction, this region of increasing pressure is called adverse pressure gradient. It reverses the flow direction and enforces the flow to move back upstream.

4.5 Results and Calculations

It is well known that Darrieus wind turbines are not self-starting due the negative torque coefficient in the tip speed ratio range of approximately 0 to 2. Therefore, bigger TSR values from 3 - 5.5 is chosen for the analysis, similar to wind tunnel test. Results are presented in table 4. The simulations of the different cases show that the turbine performance is sensitive to the placement position. Fig 40 - 41 shows the combined torque variation for all blades at the last cycle, when torque does not vary more than 1%. The repeatable oscillatory behavior is observed at each case, tip speed ratio at different positions lead to different range of minimum and maximum torque produced by the turbine. Position 3 shows bigger oscillation range compared to Position 1 and 2. Negative torque is observed at Position 3, $\lambda = 4$, this shows that the drag begins to increase as the blade enters into stall. As a result, power coefficient value is also decreased as shown in Table 4. The larger oscillation range indicates higher fatigue loading and larger mechanical vibrations. Reynolds number on chord is important non-dimensional parameter and can be used for "scale effect" study and validation. The Reynolds number for the blade chord is calculated as

$$\text{Re}_c = \frac{\lambda uc}{\nu} \tag{14}$$

Where "λ" is the tip speed ratio and "ν" is the kinematic viscosity of air. Free stream velocity is represented by symbol "u" and "c" is the blade chord length. Literature review shows lower Re_c < 10^3 will have rampant viscosity effects and typical airfoil will not transition to turbulence. The range of $10^3 < \text{Re}_c < 10^6$ is the transitional region for airfoil and wings. The laminar transitional and turbulent flows will have significant effects on the forces generated by the wings and each must be modeled accurately [50]. Based on the Eq. 14, Reynolds number for various tip speed ratios is 0.16×10^6. The Reynolds number reported for Sandia 2m wind tunnel model at different rotational speed are between $0.1 \times 10^6 - 0.3 \times 10^6$ [51]. As mentioned in table 4, the range of tip speed ratio for power production was determined to be $3 < \lambda < 5.5$ for all cases. The quadratic curve for position 1 and position 2 for given tip speed ratios follows the same trend and increases with increase in TSR. The curve declines for Position 3 with increase in tip speed ratios. The Turbine performs poorly at Position 1 and 2 for lower values of tip speed ratio.
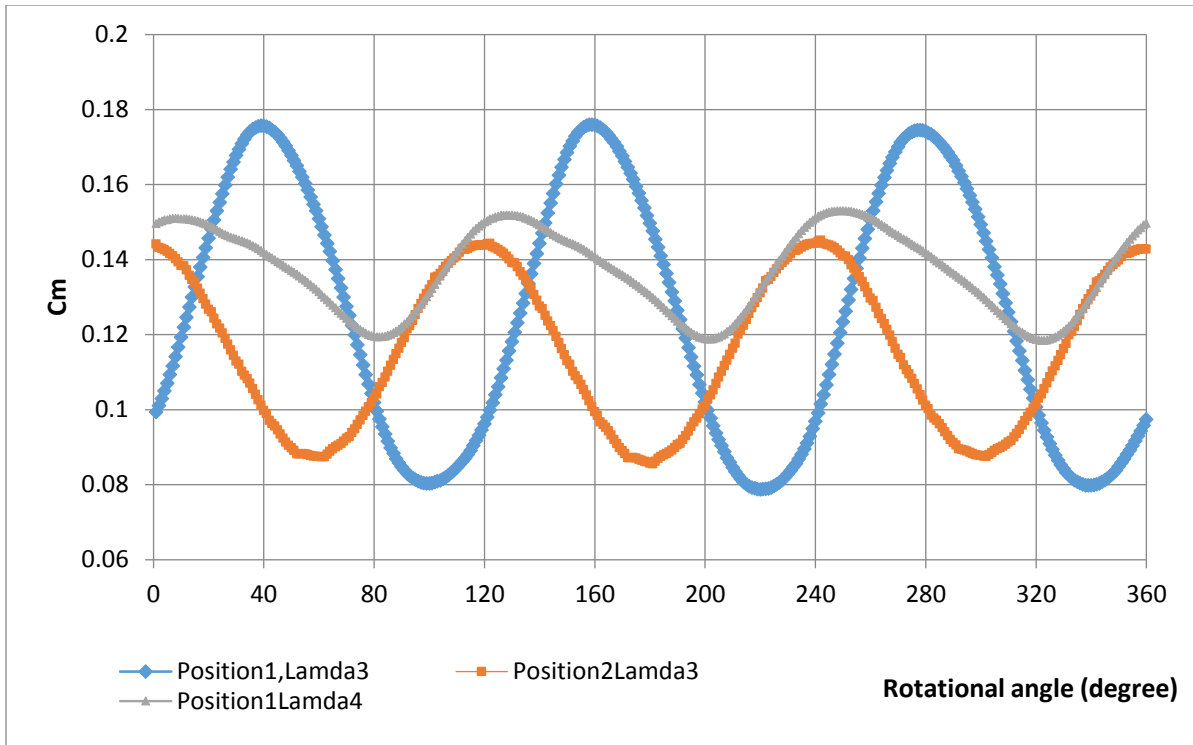
Figure 40: Instantaneous torque variations at last cycles for Position 1-2
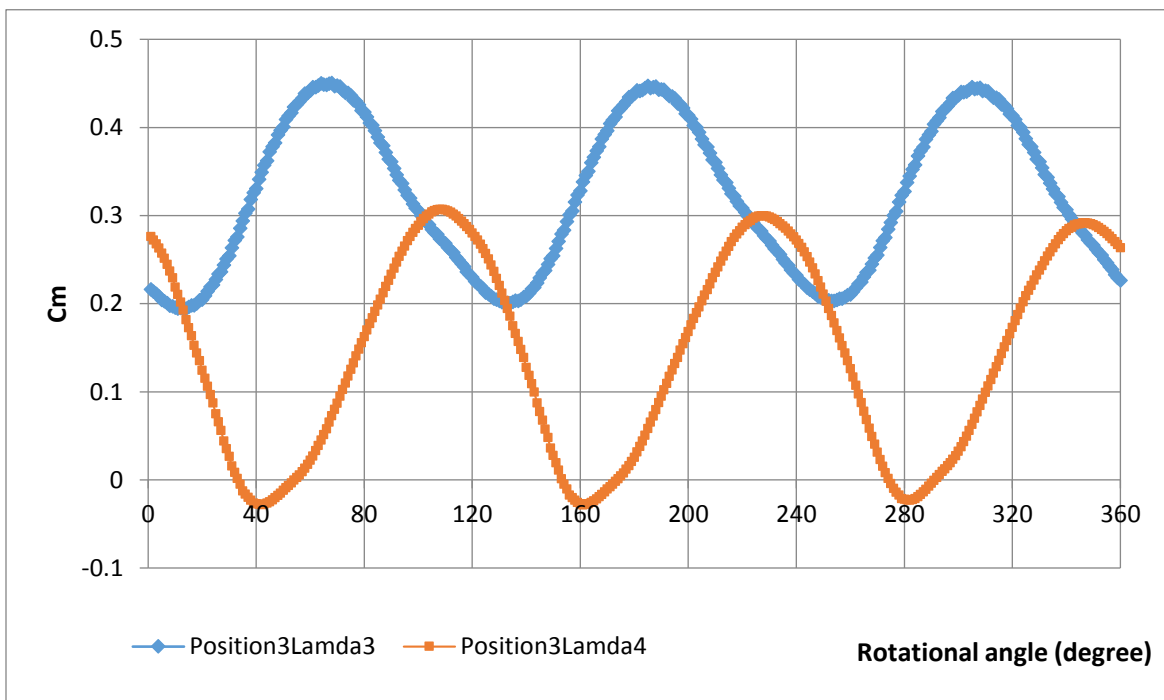
Figure 41: Instantaneous torque variation at last cycle for Position 3
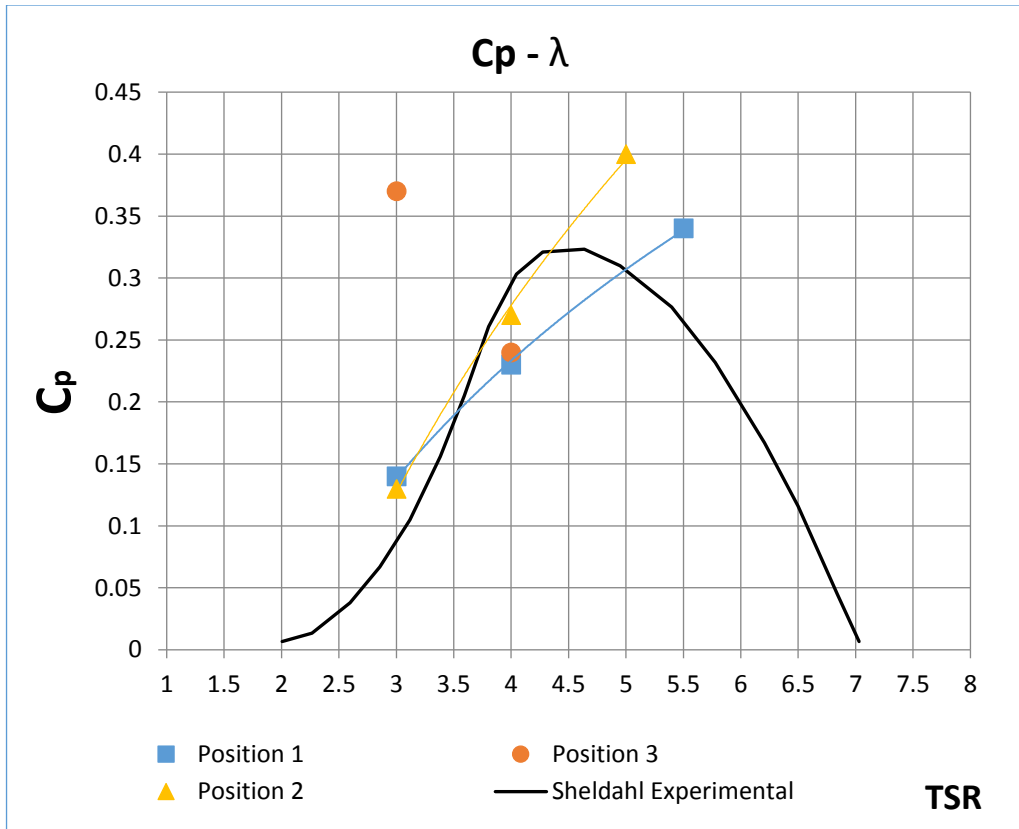
Figure 42 Cp vs. TSR Summary

The poor performance is due to overlap of separation bubble with the rotor's geometry as seen in fig. 44 - 45. For Position 1, the power coefficient has it maximum value at $\lambda = 5.5$. The value is slightly above the baseline configuration of 0.33. Position 2, $\lambda = 5$ shows a maximum value of 0.4, A significant increase of 30% higher than Sandia's wind tunnel test results. Fig. 42 shows comparative study results of all positions with Sandia's experimental results. The peak power coefficient value for Position 1 – 2 is higher than baseline configuration. The blades experience enhanced relative wind speed due to flow acceleration from the building. The convergence time and number of cycle varies for each case. Due to highly turbulent nature of flow, different pattern of vortex shedding at positions and flow around the turbine induce oscillations in the solutions. This requires more rotation to achieve a periodic torque.

For Position 1, the solution is converged after 20-35 cycles for different tip speed ratios. Position 2 takes 30 - 40 cycles for convergence. Position 3 takes the longest time comparatively and convergence is achieved after 30 - 45 cycles. For a computer equipped with 12 cores and 96G ram. It takes 35-40 days to achieve 40 cycles with time step of 1 degree.

Table 4: Power Coefficient for various Tip speed ratios

	λ = 3	λ = 4	λ = 5	λ = 5.5
Position 1 (C_P)	0.141	0.227		0.342
Position 2 (C_P)	0.133	0.272	0.40	
Position 3 (C_P)	0.371	0.235		

Figure 43 shows the pressure contours at the mid plane of the rotor for position 3. A non-uniform pressure distribution is seen around the blades. Detailed view of the airfoil on the right side shows high static pressure at the windward side of the returning blade. This is because the blades experience a combination of rotational and incoming wind velocity, yielding a total apparent wind at an angle of attack. As a result, the high and low pressure zones around the blades contribute to the torque output and aerodynamics forces. The magnitude of these forces is dependent of the incoming flow velocity and position of the blade in azimuthal plane.
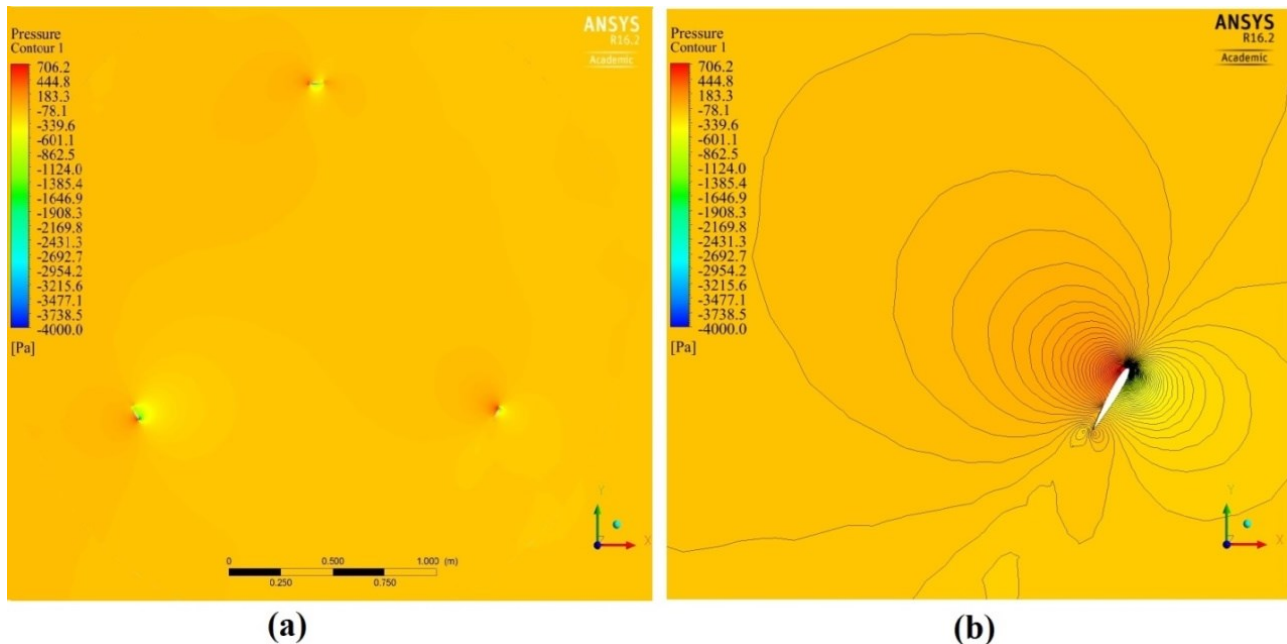
Figure 43: (a) Pressure contours at Position3 λ=3 (b) Detailed view of the blade
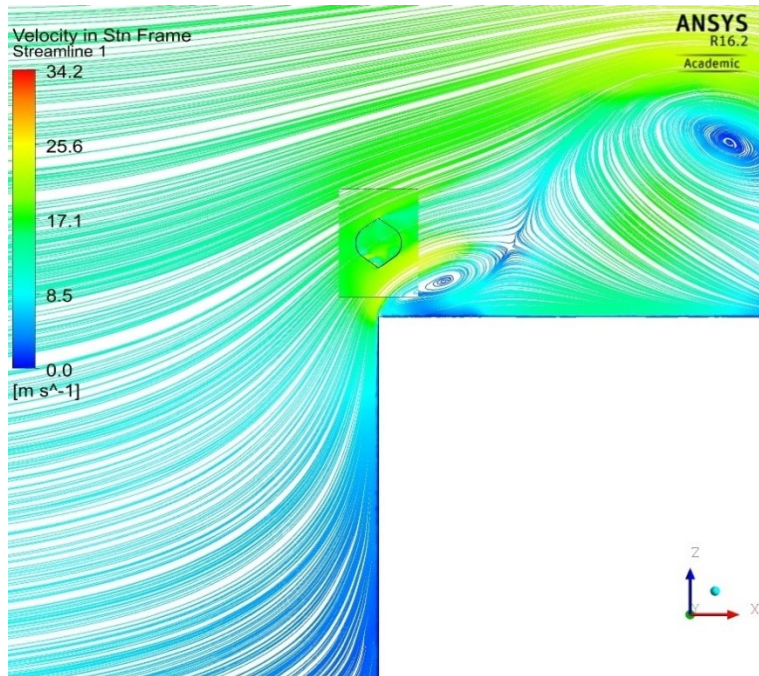
Figure 44: Streamlines (λ = 3), Position 1
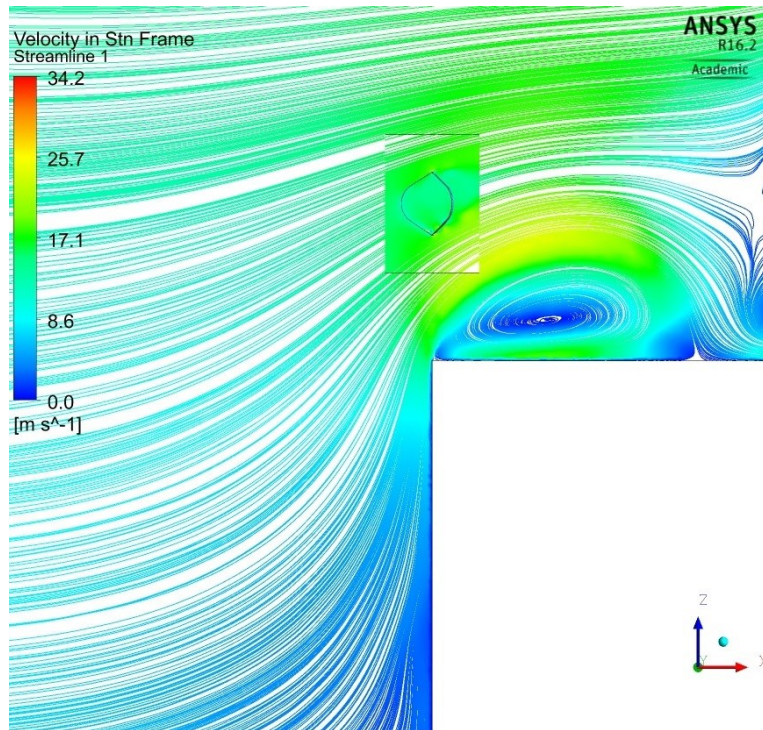
Figure 45: Streamlines (λ = 3), Position 2
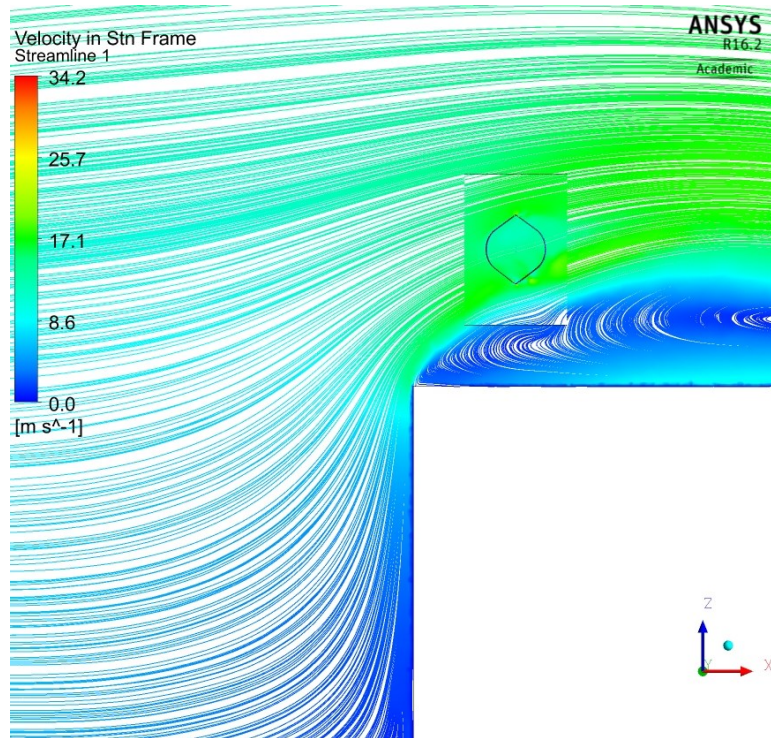
Figure 46: Streamlines (λ = 3), Position 3
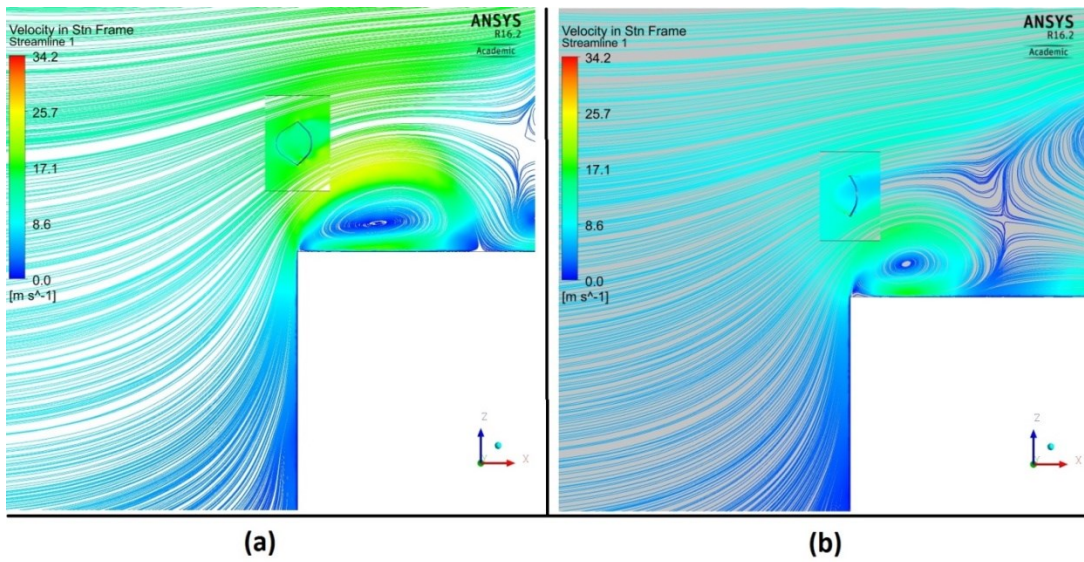
Figure 47: (a) Position 2 (λ = 3), (b) Position 2 (λ = 5)

Figure 44 - 47 shows instantaneous streamlines of velocity contours at different positions for the same tip speed ratios. To link velocity in stationary and rotating zone around the rotor, the velocity relative to stationary frame is used to plot streamlines. The color of the streamlines show the magnitude of the velocity and how flow is drawn to the swept area of the rotor. It also helps to identify flow acceleration and separation bubble at the rooftop. The contours are plotted at the plane taken at the middle of rotor, normal to y-axis. The accelerated flow enhances streamlines contraction at the upstream edge and wind velocity forms skew angle with horizontal surface of the roof. It was shown by Martens that this skew angle depends on the position at the roof, shape of the building and surrounding roughness [26]. In addition, the vortex formation on the roof is affected by the magnitude of wind velocity and turbine placement. The turbine downstream aerodynamics and the edge of the building affect the height and shape of the flow separation. Position 1 - 2, $\lambda = 3$ shows that the rotor is in highly turbulent separation bubble, practically it causes the damage by fatigue and results in poor performance of the rotor. In other words, the accelerated flow negatively affects the performance of the turbine at Position 1-2 for lower TSR's. The shape of separation bubble for the Position 1 and Position 2 is similar and deteriorates quickly without stretching across the roof. The turbine does not have much effect on the flow at position 3 as the separation bubble on roof top (figure 46) is similar to flow over a building without the turbine as shown in figure 12. For this reason, the turbine performs better for Position 3, $\lambda = 3$ and the value of power coefficient increases by 12% than baseline configuration.

CHAPTER 5: CONCLUSION

5.1 Summary

The URANS numerical analysis of roof mounted Darrieus wind turbine was studied in this thesis and results show the performance sensitivity with respect to turbine's placement position. The numerical methodology was validated with experimental results from Sandia's and numerical results from Bedon [35] . The methodology validation serves as seminal approach to identify the main parameters of the mesh, such as y^+, number of elements across the airfoil and surface of the blade. The SST k-ω turbulence model is used during validation and for the roof mounted simulation, for its accurate prediction of flow separation and good agreement with wind tunnel experimental results. The considerable difference in the numerical setup of wind tunnel and full scale roof mounted model is the replacement of uniform velocity inlet boundary condition to atmospheric boundary layer profile, to simulate realistic wind flow of urban areas.

The numerical analysis was performed for range of tip speed ratio for three different positions in proximity of upstream edge to gain advantage of flow acceleration. The height difference of different positions is a function of rotors diameter. It was concluded that all positions get benefit from upstream flow acceleration but the maximum C_p is found for different TSR values depending on the placement. The turbine performance is significantly affected by the presence of flow separation and vortex formation on the rooftop. As a result, peak power coefficient and vortex formation on the rooftop is highly dependent on rotor's placement. The power coefficient for Position 1 and 2 increases with the tip speed ratio. The lowest values for both positions is recorded at the TSR = 3, which corresponds to decrease of 120% in the rotor's performance than baseline configuration of 0.33. Position 2, TSR = 5 shows the improvement of 21 percent than baseline configuration. The C_p - λ curve for position 3 shows the reverse trend and turbine's performance drops quickly with increase in tip speed ratio. For the multi staged turbine setup, the option to install adjacent downstream turbine is unlikely due to flow separation and highly turbulent wake generated by the upstream turbine placement, but a series of these turbines can be installed along the upstream edge to harvest more wind energy.

5.2 Future work

Many assumptions are considered for this study such as flat roof of the building with no obstacle at the rooftop and no effect of any other building on the wind gradient. Furthermore, a single cube shaped building is studied, therefore different building heights should also be investigated first. Although field test results by Sandia showed identical C_p - λ curves for 400 and 460 rpm, numerical analysis for different rotational speed should be performed, for varying TSR values because the turbine is interacting with the building.

Other placement positions for turbine placement such as corners of the building should be exploited to gain advantage of flow acceleration from multiple edges at different wind directions. The results reported only take into account the turbulent effects and mechanical losses from components are not taken into account. Finally, the results should be validated against the experimental results.

In addition, changes in rotor's geometry should be analyzed. Airfoil with more blade thickness such as NACA 0015 and NACA 0018 should be utilized to support the gravitational and centrifugal loadings of the Troposkien structure. These airfoils contribute to improved structural strength of blades, but this could have the disadvantage of higher drag coefficients at lower angle of attacks. As mentioned earlier, Darrieus wind turbines are not self-starting at lower tip speed ratio of 0 to 2, this could be resolved by testing non-symmetrical airfoil such as S102. It was shown by Kirke that Darrieus type wind turbines equipped with cambered airfoil blades has self-starting capability without the help of variable pitch [52]. Numerical simulation of multiple turbines adjacently placed at the upstream edge should be performed to understand to aerodynamic interference on the performance of rotor.

REFERENCES

[1] J. Goldemberg, "The promise of clean energy," *Energy Policy,* 2006.

[2] "Annual Energy Outlook 2007 with Projections to 2030," Washington, 2006.

[3] D. J. Mackay, Sustainable Energy- without the hot air, UIT Cambridge, England, 2009.

[4] L. Fried, L. Qiao, S. Sawyer and S.Shukla, "Global Wind Report-Annual market Update," Global Wind Energy Council, Brussels, Belgium, 2015.

[5] "Energy Consumption and Conservation in the Mid and high rise Residential Buildings in British Columbia," 2012.

[6] S. Sisbot, O. Turgut, U. Camdali and M. Tunc, "Optimal positioning of wind turbines on Gokceada using multi-objective genetic algorithm," *Wind Energy,* pp. 297-306, 2010.

[7] W. Seifritz, "An endogenous technological learning formulation for fossil fuel resources," *Journal of Hydrogen Energy,* vol. 28, no. 11, pp. 1293-1298, 2003.

[8] W. White, A. Lunnan, B.Kulisic and E. Nybakk, "The role of governments in renewable energy: The importance of policy consistency," *Biomass and Bioenergy,* vol. 57, pp. 97-105, 2013.

[9] "Renewables 2010 Global Status Report," Paris, 2017.

[10] T. Ashwill and T. Leonard, "Developments in Blade Shape Design for a Darrieus Vertical Axis Wind Turbine," Sandia National Laboratories, 1986.

[11] R. Sheldahl, "Comparison of Field and Wind Tunnel Darrieus Wind Turbine Data," Sandia National Laboratory, 1981.

[12] C. Song, Y. Zheng, Z. Zhao, Y. Zhang, C.Li and H.Jiang, "Investigation of meshing strategies and turbukence models of computational fluid dynamics simulations of vertical axis wind turbines," *Journal of Renewable and Sustainable Energy,* vol. 7, no. 3, 2015.

[13] B. F. Blackwell and G. E. Reis, "Blade shape for Troposkien type of Vertical axis Wind Turbine," Sandia National Laboratories, 1977.

[14] G. Reis and B. Blackwell, "Practical Approximations to a Troposkien by Straight-Line and Circular-Arc Segments," Sandia Laboratories Energy Report, 1975.

[15] W. Tiju, T. Marnoto, S. Mat, M. Ruslan and K.Sopian, "Darrieus vertical axis wind turbine for power generation I: Assessment of Darrieus VAWT configuration," *Renewable Energy,* vol. 75, pp. 50-67, 2015.

[16] I. Paraschivoiu, Wind Turbine design with emphasis on Darrieus concept, Montrèal: Polytechnic International press, 2002.

[17] S. Kooiman and S. Tullis, "Response of a Vertical Axis Wind Turbine to Time Varying Wind Condition found within the Urban Environment," *Wind Engineering,* vol. 34, pp. 389-401, 2010.

[18] A. Das and P. K.Talapatra, "Modelling and Analysis of a Mini Vertical Axis Wind Turbine," *International Journal of Emerging technology and Advanced Engineering,* vol. 6, no. 6, 2016.

[19] D. Sahini, "Wind Tunnel Blockage Corrections," Texas Tech University, 2004.

[20] B. Phillips, P. Robertson and Nowak, "On the wake of Darrieus Turbine," University of Western Ontario, London, 1981.

[21] E. Dayan, "Wind energy in buildings," Building Research establishment, UK, 2006.

[22] L. Lu and K. Ip, "Investigation on the feasibility and enhancement methods of wind power utilization in high-rise buildings of Hong Kong," *Renewable and Sustainable Energy Reviews,* vol. 13, no. 2, pp. 450-461, 2009.

[23] C. Song and J.He, "Computation of wind flow around a tall building and the large scale vortex structure," *Journal of Wind Engineering and Industrial Aerodynamics,* Vols. 46-47, pp. 219-228, 1993.

[24] A. Weerasuriya, "Computational Fluid Dynamics (CFD) Simulation of Flow around Tall Buildings," *The Institution of Engineers, Sri Lanka,* pp. 43-54, 2013.

[25] L. P. Andrè, "CFD Based Synergistic Analysis of Wind Turbine for Roof Mounted Integration," April 2016.

[26] S. Martens, "The energy yield of roof mounted wind turbines," *Wind Engineering,* vol. 27, pp. 507-

518, 2003.

[27] R. Whittlesey, S. Liska and J.O. Dabiri, "Fish schooling as a basis for vertical axis wind turbine farm design," *BioInspiration and Biomimetic,* vol. 5, 2010.

[28] D. Weihs, "Hydromechanics of Fish Schooling," *letters to nature,* vol. 241, p. 290, 1973.

[29] D. Rekioua, Wind Power Electric Systems : Modeling,Simulation and Control, Springer, 2014.

[30] K. Busawon, L. Dodson and M Jovanovic, "Estimation of the power coefficent in wind conversion system," in *IEEE*, Seville, Spain, 2005.

[31] T. Wizelius, Developing wind power projects : Theory and Practice, 2006.

[32] D. Digraskar, "Simulation of Flow over Wind Turbines," University if Massachusetts, 2014.

[33] Ansys fluent User's guide 12.0, April 2009.

[34] K. Kim and P.A.Cizmas, "A Three dimensional hybrid mesh generation for turbomachinery airfoils," in *37 Joint Propulsion Conference adn Exhibit*, Salt Lake City, 2002.

[35] G. Bedon, E. Benini and S. Betta, "A computational assessment of the aerodynamic performance of a tilted Darrieus wind turbine," *Journal of Wind Engineering and Industrial Aerodynamics,* vol. 145, pp. 263-269, 2015.

[36] J. Tu, G. H. yeoh and C.Liu, Computational Fluid Dynamics, A pratical Approach, 2012.

[37] Ansys Fluent Theory Guide, Ansys Inc., November 2013.

[38] J. Piquet, Turbulent Flows: Models and Physics, Springer, 1999.

[39] S. Pope, Turbulent Flows, Cambridge University Press, 2000.

[40] S. Patankar and D. Spalding, "A calculation procedure for heat, mass and momentum transfer in three-dimensional parabolic flows," *Journal of heat and mass transfer,* vol. 15, no. 10, pp. 1787-1806, 1972.

[41] L. Mangani and C. Bianchini, "Heat Transfer Applications in Turbomachinery," in *OpenFOAM conference*, London, 2007.

[42] M. Milanese, A. d. Risi and D. Laforgia, "Performance Optimization of Building Integrated-Mounted Wind Turbine," *Applied Mechanics and Materials,* Vols. 260-261, pp. 69-76, 2013.

[43] A. Peacock, D. Jenkins, M. Ahadzi, A. Turan, Berry and S., "Micro wind turbines in the UK domestic sector," *Energy and buildings,* vol. 40, no. 7, pp. 1324-1333, 2007.

[44] L. Ledo, P. Kosasih and P.Cooper, "Roof mounting site analysis for mirco-wind turbines," *Renewable energy,* vol. 36, no. 5, pp. 1379-1391, 2011.

[45] P. Blackmore, "Building-mounted Micro-wind Turbines on High-rise and Commerical Buildings," 2010.

[46] S.Shawn, R. Alyssa, B. David and K.Dave, "Status Report on Small Wind Energy Projects Supported by Massachussets Renewable Enegy Trust," MIT, 2008.

[47] F. Balduzzi, A. Bianchini, E. Carnevale, L. Ferrari and S.Magnani, "Feasibility analysis of a Darrieus vertical-axis wind turbine installation in the rooftop of a building," *Applied Energy,* vol. 97, pp. 921-929, 2012.

[48] M. Kinzel, Q. Mulligan and J.O.Dabiri, "Energy exchange in an array of vertical-axis wind turbines," *Journal of Turbulence,* vol. 13, pp. 38-39, 2013.

[49] Y. Tominaga, A. Mochida, R. Yoshie, H. Kataoka, T. Nozu, M. Yoshikawa and T. Shirasawa, "AIJ guidelines for practical applications of CFD to pedestrian wind environment around buildings," *Journal of wind engineering and Industrial Aerodynamics,* vol. 96, no. 10-11, pp. 1749-1761, 2008.

[50] J. McArthur, "Aerodynamics of wings at low reynolds number," University of Southern California, 2007.

[51] R. Sheldahl and P. Klimas, "Aerodynamics Characteristics of Seven Symmetrical Airfoil Section Through 180-Degree Angle of Attack for Use in Aerodynamic Analysis of Vertical Axis Wind Turbines," Sandia National Laboratories, 1981.

[52] B. Kirke, "Evaluation of Self Starting Vertical Axis Wind Turbines for Stand Aline Applications," Griffith University, 1998.